# HARVARD UNIVERSITY
## Graduate School of Arts and Sciences
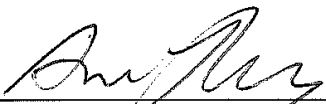
## DISSERTATION ACCEPTANCE CERTIFICATE

The undersigned, appointed by the

School of Engineering and Applied Sciences

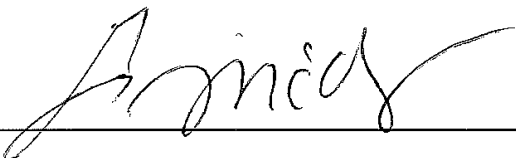have examined a dissertation entitled:

"Imaging Electron Flow in Graphene"

presented by : Sagar Bhandari

candidate for the degree of Doctor of Philosophy and here by certify that it is worthy of acceptance.

Signature _____

Typed name:  Professor A. Yacoby

Signature _____

Typed name:  Professor M. Loncar

Signature _____

Typed name:  Professor E. Heller

Signature _____

Typed name:   Professor R. Westervelt

Date  May 4, 2015

# Imaging Electron Flow in Graphene

A dissertation presented

by

Sagar Bhandari

to

School of Engineering and Applied Sciences

in partial fulfillment of the requirements
for the degree of
Doctor of Philosophy
in the subject of
Applied Physics

Harvard University
Cambridge, Massachusetts

May 2015

Thesis advisor

**Robert M. Westervelt**

Author

**Sagar Bhandari**

# Imaging Electron Flow in Graphene

# Abstract

Scanning probe techniques can be used to probe electronic properties at the nanoscale, to shed light on the physics of nanoscale devices: Graphene is of great interest for its promise in both applied(e.g. spintronics and valleytronics) and fundamental research (e.g. quantum Hall and Dirac fermions). We successfully used a cooled scanning gate microscope to image the motion of electrons along cyclotron orbits for magnetic focusing in graphene. Part of my time at Harvard was also spent incorporating a low temperature scanning capacitance setup into the existing microscope as well as building a low temperature coarse positioning system.

To image magnetic focusing of electrons in graphene, a conducting tip of a scanned probe microscope is held just above the sample surface, and an applied tip-to-sample voltage creates an image charge that is moved while the transresistance between two leads is measured. The sample is a high mobility hBN-graphene-hBN sandwich etched into hall bar geometry with two point contacts along each side. By tuning the transverse magnetic field B and electron density n in the graphene layer, we observe the first few magnetic focusing peaks. For values of B and n that correspond to the first magnetic focusing peak, we observe an image of the cyclotron orbit that extends from one point contact to the other. We also study the effects of B and n on

the spatial distribution of electron trajectories as we move away from the magnetic focusing peak.

We also present the design and implementation of a cooled scanning capacitance probe that operates at liquid He temperatures to image electrons in nanodevices. In this setup, an applied sample-to-tip voltage creates an image charge that is measured by a cooled charge amplifier adjacent to the tip. The circuit is based on a low-capacitance, high-electron-mobility transistor(HEMT) (Fujitsu FHX35X). The input is a capacitance bridge formed by a low capacitance pinched-off HEMT transistor and the tip-sample capacitance. We have achieved a low noise level ($0.13$ e$/\sqrt{Hz}$) and high spatial resolution (100 nm) for this technique, which promises to be a useful tool to study electronic behavior in nanoscale devices.

# Contents

# List of Figures

# Dedication

My father has always been an inspiration in my life. His words of encouragement in the pursuit of excellence are still lingering in my thought. Only through his dedication and sacrifices was i able to reach several important milestones. He always had confidence in me and was very supportive of my choice of studies. In later years of his life, he was very proud that his son was working towards a PhD.

I am very sorry that my father did not get to see the completion of my PhD. Although he may not have had a grasp of what i was working on, he along with my mother and my sister were unwavering supporters through the years. So it is with great pride and affection that I dedicate this dissertation to my father, Gopal Pd. Bhandari (1958-2013)

# Acknowledgments

First and foremost, I would like to sincerely thank my supervisor Bob Westervelt for his guidance and support throughout my PhD, and especially for showing confidence in me. His understanding, encouragement, and mentorship during my time at Harvard has been a blessing.

I would like to thank my committee members, Eric Heller, Amir Yacoby and Evelyn Hu for their guidance throughout my work. Thanks to Marko Loncar for being available at late notice to serve on my committee.

Thank you to all my colleagues from the Westervelt lab; my close friends, Kevin Tian, Caspar Floryan, and Ben Yang, for their friendship, support, and guidance; Andrew Lin, for his enthusiasm ; Estelle Cohen for her energy and optimism. Additionally, I greatly appreciate the invaluable mentorship and support i received from the seniors in Westervelt Lab, Halvar Trodahl, Erin Boyd, and Jesse Berezovsky.

I am very grateful to all those who have supported my research during my time here at Harvard; Naomi Brave, for her extraordinary work in keeping the lab running smoothly, Stan Cotreau in helping me with machining in the Physics Machine Shop; and the CNS for running the cleanroom, imaging suite, and other facilities.

I am forever indebted to my family for the love and support they provide. The sacrifices they have made giving me the opportunity to pursue my interests in sciences are second to none. Thank you to my Late father Gopal Pd. Bhandari, mother Gita Bhandari, and my sister Junu Bhandari.

# Chapter 1

# Introduction

In semiconductor research, the scientific community has been working towards two primary goals - miniaturization of electronics and incorporation of novel materials. This has opened up paths to new potential applications such as nanoscale computing, spintronics and quantum information processing. To better design these novel electronics, it would be important to study and understand the fundamentals of such devices.

The miniaturization has brought the size down to nanoscale over the course of several decades. As the devices become smaller, quantum mechanical effects become more relevant. Non-classical phenomena such as coherence, interference and wave like properties of electrons start appearing at this scale.

Primary measurement techniques used for studying these devices are bulk measurement techniques such as electronic transport measurement and photoluminescence which aren't sufficient to reveal the local variation of material properties at smaller length scales. To understand the subtleties in electronic properties of such

nanoscale devices, it would be critical to perform local measurements of transport properties at similar length scales. Scanning probe techniques are the tools that allow us to study such local sample properties in length scales ranging from few atoms to several nanometers. To mention a few, scanning probe techniques such as atomic force microscopy, scanning tunneling microscopy all reveal these local electronic and/or mechanical properties of sample at nanometer scale.

One of such scanning probe technique is scanning gate microscopy, pioneered by the Westervelt lab over the last decade [1, 2]. This technique has been used for studying the local electronic properties of materials such GaAs/AlGaAs heterostructures, InAs/InP nanowires, and graphene. The nanoscale devices that are studied can be divided into two main categories - closed and open systems. In closed systems, electrons are confined and it would be possible to manipulate an individual charge or spin while in open systems the transport is dominated by the ballistic motion of electrons. My research in Westervelt lab, focused on using the scanning gate measurement technique to image flow of electrons in open systems such as graphene. As part of my research, I also worked on incorporating another scanning probe technique that measures local spatial variation in capacitance in nano devices.

## 1.1   Scanning Gate Microscopy

In a scanning gate measurement, local trajectories of electrons can be mapped in the sample by having a conducting tip directly above it raster scan the sample while simultaneously measuring the conductance change through the sample. The tip scatters the electrons locally affecting the conductance of the sample and hence,

the conductance map reveals the electronic trajectories in the sample. The first experiment done in Westervelt lab that demonstrates such capability was imaging of ballistic motion of electrons through a quantum point contact in GaAs/AlGaAs heterostructures.
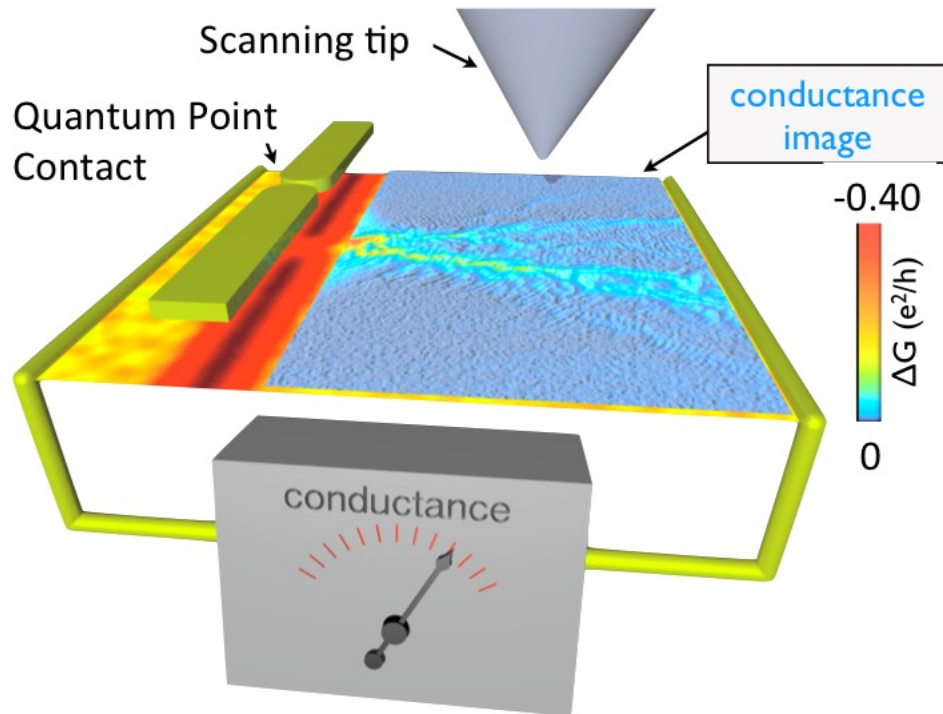


Figure 1.1: Illustration of a scanning probe setup in imaging ballistic flow of electrons through a quantum point contact in two dimensional electron gas.The tip voltage depletes a small divot in the electron gas below, that scatters electron waves back through the QPC, reducing its conductance. By displaying the QPC conductance as the tip is raster scanned across the sample, and image of electron flow is obtained.

The schematic diagram in Fig. 1.1 shows how an image of electron flow is recorded using a scanning gate microscope. The tip voltage depletes a small divot in the electron gas below, that scatters electron waves back through the QPC, reducing its conductance. By displaying the QPC conductance as the tip is raster scanned across the sample, and image of electron flow is obtained. The maps of electron trajectories

revealed fringes corresponding to the interference of electron waves. The fringes were spaced at half a fermi wavelength confirming the existence of coherent waves of electrons in 2DEG. After the first experiment, scanning gate microscopy has been used in probing the motion of electron waves in (2DEGs) ,[1, 2, 3, 4, 5, 6, 7, 8] and also to manipulate electrons confined in quantum dots in semiconductor nanowires,[9, 10, 11] carbon nanotubes,[12, 13] and graphene.[14, 15, 16, 17]
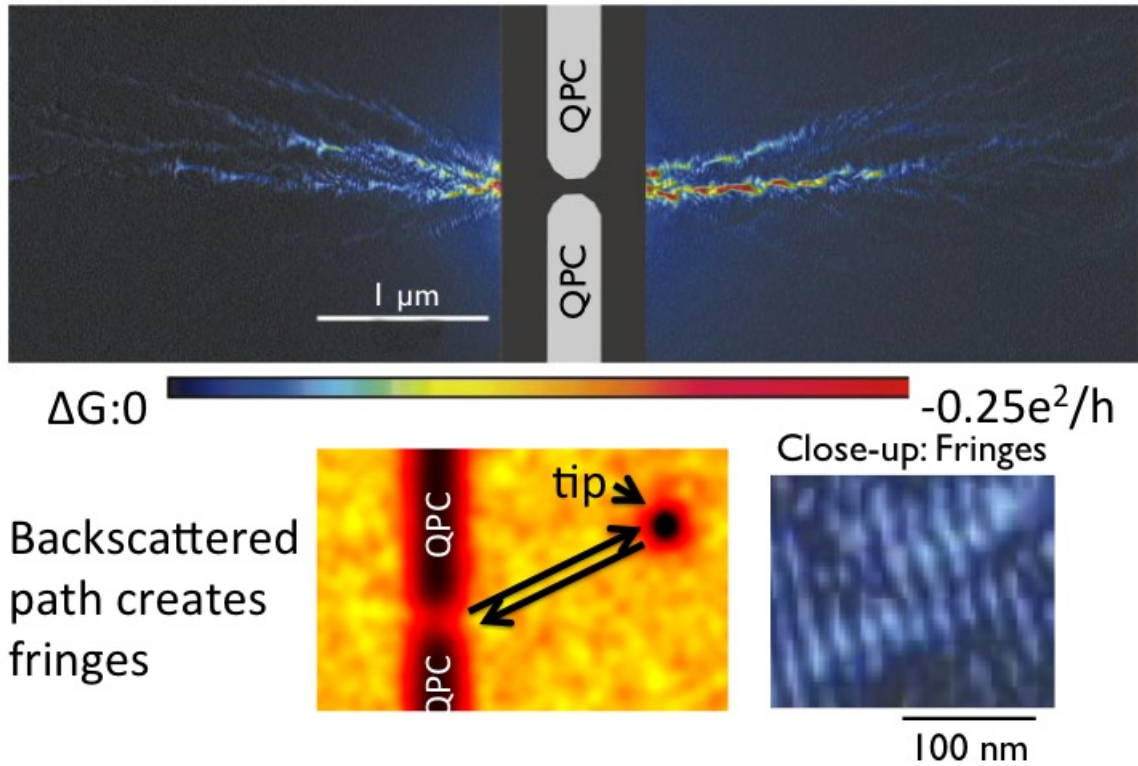


Figure 1.2: Scanning gate microscopy images of the electron flow through a quantum point contact. The images reveal the interference fringes appearing at half the fermi wavelength which verifies that the electron waves are coherent at the this length scale. These images were adapted from [2].

The experiment that motivated my work was the imaging of magnetic focusing of

electrons in two dimensional electron gas in GaAs/AlGaAs heterstructures [6]. Using scanning gate technique flow of electrons between two QPCs in a 2DEG , at the first and second magnetic focusing peaks were mapped in this experiment. Electron transmission between two quantum point contacts peaks when the distance between the two QPCs is an integer multiple of the cyclotron diameter. Figure 1.3 is an image of the cyclotron orbit of electrons in a GaAs/AlGaAs 2DEG recorded on the first magnetic focusing peak.
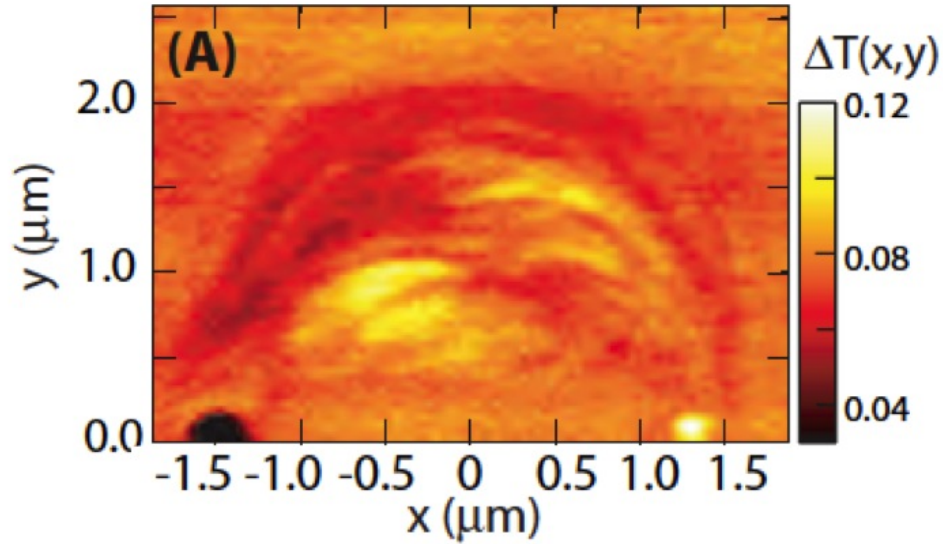


Figure 1.3: Scanning gate images of magnetic focusing of electrons in two dimensional electron gas in GaAs/AlGaAs heterostructures. The image shows the trajectories of electrons, near the first focusing peak. The trajectories are between two QPCs (dark and light region). Image adapted from [6].

My work in Westervelt lab involves imaging of magnetic focusing of electrons in graphene. Unlike 2DEG in a GaAs/AlGaAs, graphene is a naturally occurring

two dimensional system with the electrons freely moving on its surface. This makes graphene an ideal testbed for scanning probe techniques. Figure 1.4 shows the electron trajectories in graphene device when a perpendicular magnetic focusing field is applied.
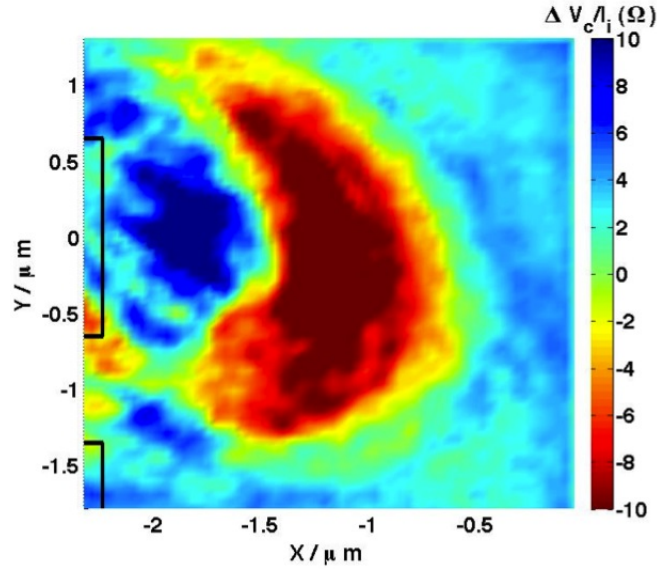


Figure 1.4: Experimental image of magnetic focusing in grapheme, near the first focusing peak, revealing the electron trajectories from one narrow lead to another (dark line on the left side). This image is obtained by using the tip to slightly deflect electrons, changing the transmission between the two leads. See Chapter 4 for details.

## 1.2   Scanning Capacitance Microscopy

In Westervelt lab, I also worked on incorporating scanning capacitance microscopy (SCM) into our current setup. Before, discussing my work on scanning capacitance technique, it would be important to provide some background on SCM.

Scanning capacitance microscopy is a scanning probe technique where the spatial variation of capacitance between the probe and sample is measured. In this technique,

a conducting tip is held above the nanostructure, and an applied tip voltage creates an image charge that is measured by a cooled charge amplifier connected to the tip. By detecting changes in the image charge as the tip voltage is oscillated, local transport can be measured. Using SCM, incompressiblity of electrons can be measured locally in sample. This technique was pioneered by Ray Ashoori at MIT and has been used to image quantum hall states in 2DEGs. In 2DEGs, Quantum Hall plateaus are thought to occur as a result of localization of electrons. This can create areas of localized or delocalized electrons in 2DEG in the quantum hall regime. Using SCM, these regions where electrons could flow in or out easily (compressible) regions and regions where electrons cannot flow in or out readily (incompressible) regions were mapped in a 2DEG at a resolution of 40 nm. In our lab we plan to use scanning capacitance microscopy to probe electronic transport in small structures composed of graphene and other quantum materials.

As a proof of concept, we have been able to image the local change in capacitance in a metal electrode deposited on wafer. As shown in Figure 1.5, the change in capacitance is in the order of tens of attofarads and it verifies that we have achieved the sensitivity necessary to probe more subtle electronic properties in devices. See Chapter 4 for more details on the design and implementation of the SCM technique.
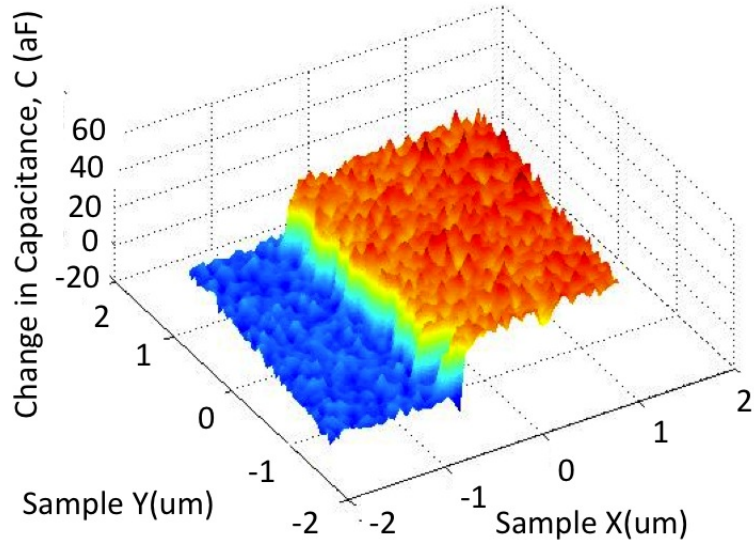
Figure 1.5: Experimental image of scanning capacitance microscopy on a gold electrode in Silicon wafer. The height of plot represents change in capacitance (aF) as the tip is scanned at a height of 20 nm on top of the edge of the 15 nm gold plate. The change in capacitance is 30 aF. See Chapter 4 for details.

## 1.3   Outline of Thesis

This thesis presents scanning gate microscopy images of magnetic focusing of electron in graphene at liquid He temperatures. In addition we describe the design and implementation of a low temperature scanning capacitance microscope.

Chapter 2 "Graphene" discusses the electronic properties of Graphene. The discussion moves from the basic electronic properties to cyclotron orbits in graphene.

Chapter 3 "Cooled Scanning Probe Microscope Apparatus" discusses the design of the low temperature coarse positioning system. This includes the discussion of the new headassembly, tip holder, cage assembly and the xy feedthroughs.

Chapter 4 "Cooled Scanning Capacitance Microscope" starts with discussion of

the cooled preamp circuit to locally image the change in capacitance at nanoscale. It presents the design and implementation of the capacitance microscopy with simulation and experimental results.

Chapter 5 "Imaging Magnetic Focusing of Electrons in Graphene" presents scanned gate microscope image of electron flow for magnetic focusing in graphene at liquid He temperatures. The images are qualitatively in good agreement with theory. The high mobility boron nitride / graphene / boron nitride devices were fabricated by Gil-Ho Lee in Philip Kim's group.

Chapter 6 "Summary and Future Experiments" contains concluding remarks, future experimental directions, and possible improvements to the low temperature scanning capacitance microscope.

# Chapter 2

# Graphene

## 2.1 Introduction

In this chapter we will discuss the electronic properties of graphene and theoretical background on magnetic focusing of electrons in graphene. We will also discuss the theory on Scanning Capacitance technique at the end of the chapter.

Graphene is a two dimensional hexagonal lattice made out of carbon atoms arranged in a honeycomb structure. It's the first two dimensional material discovered. Graphene has different allotropes in nature such as fullerenes (wrapped up graphene), carbon nanotubes (rolled graphene), and graphites (stacked graphene). Graphite can be thought of as stacks of graphene layers that are coupled by weak Van der Waals interactions. Graphene was first isolated from graphite in 2004 [18]. It was somewhat an unexpected discovery because of the predicted instability of two-dimensional crystals [19, 20].

## 2.2 Electronic properties of graphene

Graphene is a semimetal or zero-gap semiconductor. Unlike traditional semi-conductors, where the electrons have quadratic dispersion relation, the electrons in graphene have energies linearly related to their momentum at low energies. This comes out from using simple tight binding model to compute the band structure in graphene, first derived by Wallace in 1946 [21].
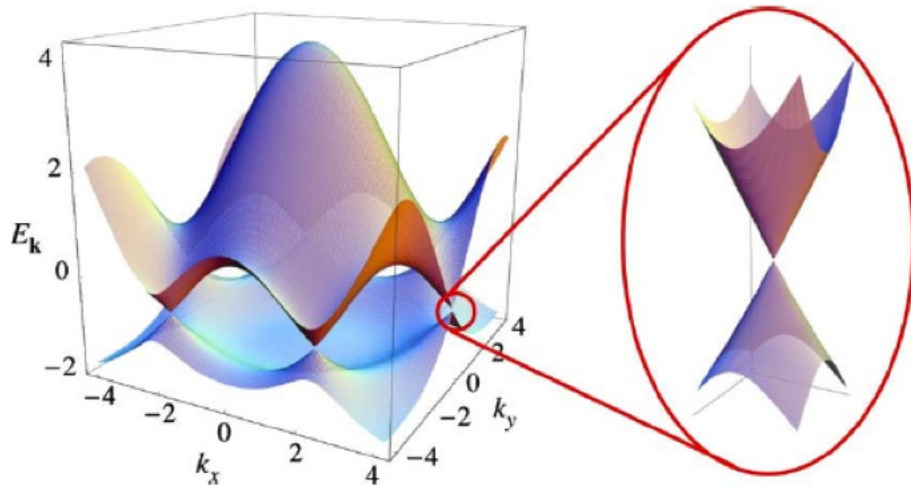


Figure 2.1: Band structure of graphene showing the linear dispersion relation at lower energies. Image adapted from [22].

Because of this linear dispersion at low-energies, the excitations in graphene are massless, chiral, Dirac fermions - these excitations follow the Dirac equation in Quantum Electrodynamics (QED) for massless fermions. The only difference is that the Dirac fermions in grapheme move 300 times slower than the speed of light c. Experi-

mentally, it's ideal to probe these low energy electrons because the chemical potential lies at the dirac point in pristine, undoped grapheme. Therefore, graphene can be an ideal testbed for probing many properties of dirac fermions in QED at smaller speed. These properties include Anomalous Quantum Hall effect, Klein tunneling and Berry's phase, to mention a few [23, 24, 25].

When dirac fermions are subjected to magnetic fields, unlike regular two dimensional electron gas, the hall conductivity $\sigma_{xy}$ is a series of equidistant steps which exists through the chargeeutrality point (Dirac point). In standard quantum hall effect, the steps occur at $\sigma_{xy} = \pm\frac{Ne^2}{h}$ where N is the Landau level index. Compared to the standard Quantum Hall effect, the series of steps in grapheme are shifted by $\frac{1}{2}$, such that $\sigma_{xy} = \pm 4e^2/h(N + \frac{1}{2})$ . There is factor of 4 appearing, with a factor of 2 from the electron spin and factor of 2 from the pseudospin associated with the two valleys.

This half-integer Quantum Hall effect in graphene can be alternatively explained by exploiting the coupling between pseudospin (which exists in graphene) and momentum. This coupling gives rise to a geometrical phase of $\pi$ when dirac fermions are moving along cyclotron trajectories in presence of magnetic field. This additional phase of $\pi$ is called Berry's phase and contributes to $\pi$ phase shift in quantum oscillations and, therefore, a half-integer shift in the Quantum Hall regime.

Another property of electrons in graphene that is very unconventional is called Klein tunneling. Unlike ordinary electrons in 2DEG, electrons in graphene can be transmitted though a potential barrier with probability 1. The angular dependence of scattering of electrons through a finite potential barrier in graphene is illustrated

in Figure 2.2.
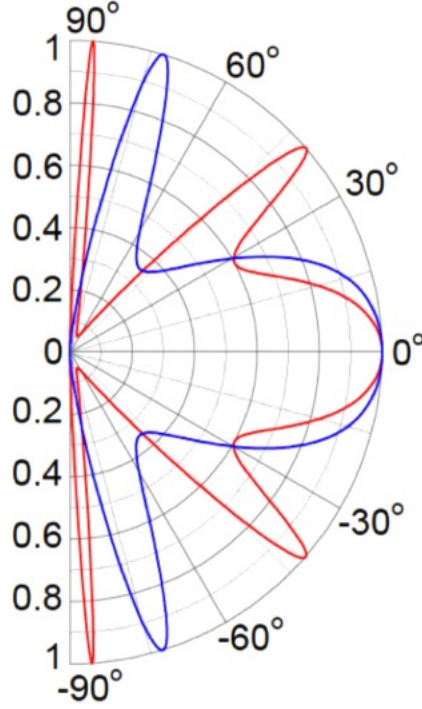


Figure 2.2: Angular dependence of transmission probability of electrons across a finite potential barrier in graphene. The red and blue curve represents the transmission when barrier heights are 200 and 50 meV respectively. The density of electrons used for this calculation was $0.5 \times 10^{12} cm^{-2}$. It can be noticed that the transmission probability is 1 when the electron is incident normal the barrier. Image adapted from [26].

As shown in Figure 2.2, the electrons in graphene have unusual characteristic of passing through potentials without getting backscattered. This can be understood in terms of conservation pseudospin and chirality. Pseudospin refers to the phase difference in the electronic wavefunctions at the two sublattices in graphene and in absence of any short-range potential that discriminates between sublattice A or B, pseudospin is essentially conserved. In addition, electrons in graphene are chiral which means pseudospin is locked into the momentum of electron. Therefore, when

a electron in graphene is incident at normal on a barrier, the initial momentum of electron is unaffected as the pseudospin cannot be flipped. This would mean that the electron would have a transmission probability of 1 at normal incidence. This property of electrons in graphene has many implications, such as observation of percolated electron and hole "puddles" [27] at charge neutrality point which suppress localization unlike in regular 2DEG , propagation of electrons without scattering over large distances.

In addition to these properties, graphene electrons have unusual traits at the boundaries. Zigzag edges can sustain edge states while armchair cannot [28]. At the boundaries, the conductance of graphene gets affected by the leads connected to it. There have been theories suggesting that the chiral Dirac nature of excitations in graphene can be used for applications where one can control the valley flavor of the electrons. [29]. Similarly, having superconducting leads connected to graphene has effects such as andreev reflection at the boundaries, and super current in graphene due to proximity effect. Various other traits such as Universal conductance fluctuations, weak localization, ahronbov-bohm effect have all been observed in graphene. [30, 31].

## 2.3 Fabrication of High quality graphene samples

The progress in fabrication technique for graphene has made it possible to explore these great variety of interesting properties of graphene. Since, the isolation of graphene for the first time in 2004, much progress has been made in the quality of graphene devices.

Since graphene is two dimensional material with it's surface completely exposed to the environment, the surfaces of graphene and it's interface with a substrate play important roles in its electronics properties. Initially, when graphene was first isolated, an $SiO_2$ layer on Silicon was used as a substrate. Graphene devices on silicon substrates have a mobility that is typically limited to 10,000 cm$^2$/Vs. In a Silcon substrate, charged impurities in corrugations, defects and adsorbates heavily scatter the electrons leading to mean free path in order of 100 nanometers. This results in the formation of electron-hole puddles near the dirac point and doping of the electron gas away from the charge neutrality point.

Efforts have been made on using different oxides as an alternative to $SiO_2$ but these surface effects tend to be universal among the oxides [32]. Getting rid of the substrate completely and having graphene suspended freely drastically improves the mobility to 200,000 cm$^2$/Vs. However, it limits the device architecture and functionality.

Hence, search for alternative substrate for graphene has undergone much research and hexagonal boron nitride (h-BN) substrates have looked promising in the recent years[32]. Hexagonal boron-nitride (h-BN) is an insulator with a hexagonal lattice structure similar to graphene with boron and nitrogen atoms replacing the carbon atoms in A and B sublattices. Because of the difference in the onsite energies of the B and N atoms, there is a large $(5.97eV)$ band gap and a small $(1.7\%)$lattice mismatch relative to graphene. It turns out that h-BN is relatively inert and free of dangling bonds due to the strong, in-plane bonding of the planar hexagonal lattice structure. Not only does h-BN have good insulating properties, it also serves as a good gate dielectric with dielectric constant of 3-4 and a breakdown voltage of 0.7 V/nm. The

preparation of graphene-hBN samples involves stacking of one layer on top of the other mechanically. Since the fabrication of graphene on BN heterostructures, many interesting properties have been discovered including the fractional quantum Hall effect, Fabry Perot oscillations and transverse magnetic focusing [33, 34, 35]. This demonstrates that graphene devices on h-BN exhibit enhanced mobility in the order of 200,000 cm$^2$/Vs, reduced surface charge and doping in comparison with graphene on SiO$_2$.

## 2.4   Transverse Magnetic focusing in Graphene

In Chapter 4, we will be presenting the images of magnetic focusing in graphene. Figure 2.3 shows how magnetic focusing occurs. The paths of electrons injected from a point contact at the origin are bent by the perpendicuar magnetic field B into circular cyclotron orbits of radius r$_c$. Electrons entering at different directions group together a cycltron diameter away, creating a dense flow into the second point contact located at this distance.

These electrons form cyclotron trajectories with radius $r_c$ in presence of magnetic field B. At certain B-field, the electron trajectories get focused on the quarter of a circle with radius $2r_c$. At the focusing point, the electron density becomes singular.

As the B field is further increased, as shown in Figure 2.4, the radius of the cyclotron motion becomes shorter and therefore, the electrons start getting reflected off the boundary. If the reflection is specular, the electrons follow skipping orbits that focus again at integer multiples of the cycltron diameter 2r$_c$, and transmission of electrons from the first to the second point contact peaks, whenever their spacing L is

an integer multiple of the cyclotron diameter $2r_c$. Since the reflection in graphene is specular, it causes the electrons to form skipping orbits which results in focal points at integer multiples of $2r_c$. The magnetic field $B_f$ required to magnetically focus electrons between two point contact separated by a distance L is

$$B_f = (\frac{2\hbar\sqrt{\pi n}}{eL})p \qquad (2.1)$$

where, $\hbar$ is planck's constant, $n$ is the electron density, $e$ is the electronic charge and p-1 is the number of reflections off the edge .
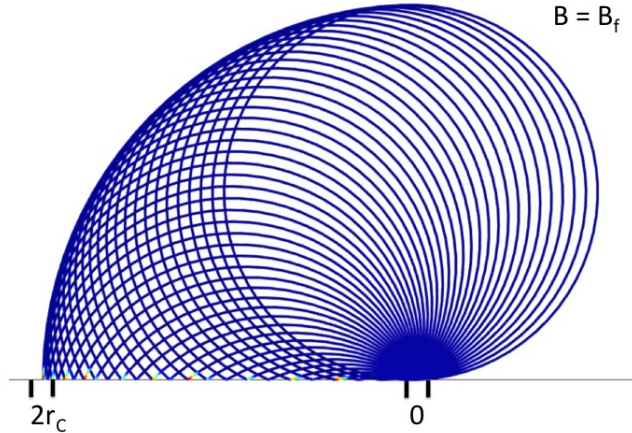


Figure 2.3: Classical trajectories of electrons injected isotropically from a point source at origin when the applied B field is at first focusing peak. The trajectories of electrons get focused at a distance equal to the cyclotron diameter from the origin.

When magnetic focusing occurs, an increase in the chemical potential in the receiving point contact starts to occcur, due to the high flow of electrons at this distance from the injecting point contact. If the receiving contact is connected to a voltmeter, which draws no current, the increase in potential is simply the voltage required to drive the same current the opposite direction into the electron gas, courtesy of the

principal of detailed balance. One can experimentally measure magnetic focusing in this way.

Similarly, as shown in top of Figure 2.4, when the B-field is increased to be B' = $2B_f$, the electrons are focused at a distance $4r'_c$ after getting specularly reflected off the edge at a distance $2r'_c$. The field B' is twice as large and the cyclotron radius r'$_c$ is half the size as r$_c$ in Figure 2.3. The bottom figure in Figure 2.4 shows the electron trajectories when a field B'=$3B_f$ is applied. In this case, the electrons get reflected twice at distances $2r"_c$ and $4r"_c$ on the edge, before getting focused at a distance $6r"_c$.
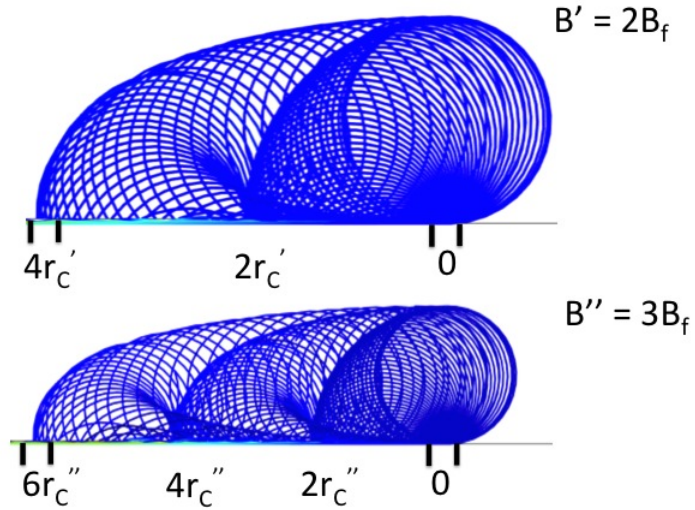


Figure 2.4: Classical trajectories of electrons injected isotropically from a point source at origin when the applied B field is at second and third focusing peaks. The first figure shows the trajectories at second magnetic focusing peak where the electron paths are focused on the edge at a distance $2r'_c$ from the origin, get specularly reflected and get focused at a distance $4r'_c$. In the second figure, at three times the field, the electrons make a double bounces at $2r_c"$ and $4r_c"$ respectively from the edge to be focused at a distance $6r_c"$.

In our experiment, we use a 20 nanometer radius conducting atomic force microscope (AFM) tip to create a movable gate above the graphene surface. The electronic trajectories get scattered from the potential so created by the tip. By simultaneously measuring the conductance through the sample as we move the tip, we map the magnetic focusing trajectories in graphene.

Figure 2.5 shows a simple simulation of the tip scattering the electron trajectories. The density dip below the tip scatters cyclotron orbits that would have hit the second point contact to other locations and thereby reduces the height of the magnetic focusing peak. One can see the shadow behind the tip's location. By diverting the flow of electron the density perturbation beneath the tip maps the electron flow which gives rise to magnetic focusing location.
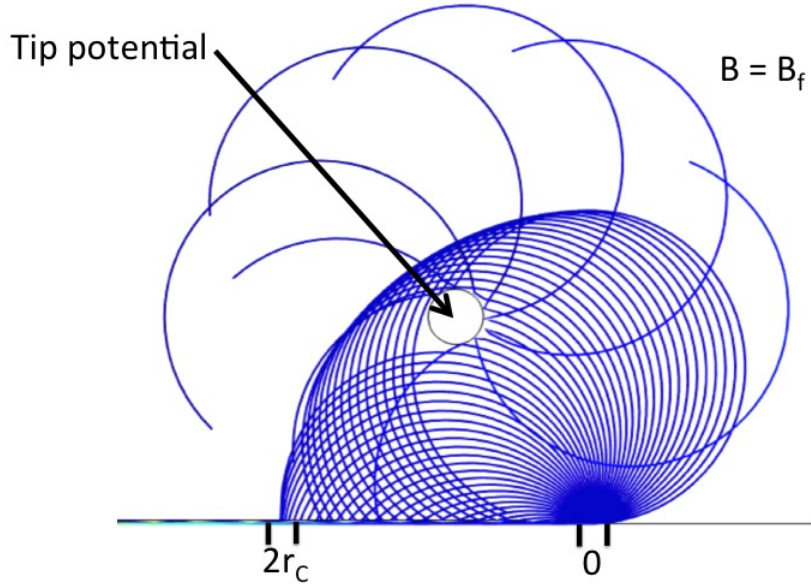
Figure 2.5: In Scanning gate microscopy, a 20 nm radius tip is brought very close to the sample surface which in turn creates a local potential on the surface. The potential acts as a movable scatterer and deflects the trajectories of electrons. Hence, as the tip is scanned over the sample, the change in conductance measured between the source and drain yields the map of electron trajectories in the sample.

## 2.5    Scanning Capacitance Microscopy-Theory

Scanning Capacitance Microscopy (SCM) provides a way to probe the conductance and quantum states of a sample without making direct physical contact. It is very useful in the study of new materials and nanoscale samples. Ashoori's group has used SCM to map Landau levels of a GaAs/AlGaAs 2DEG in the quantum Hall regime [36]. Scanning capacitance microscopy can map local transport in a two-dimensional system, it can locate and tune a quantum dot, and it can measure the so-called quantum capacitance associated with the occupation of quantum states.

A simple model of SCM of a narrow graphene channel is shown in Figure 2.6. The conducting AFM tip is capacitively coupled to the resistive channel via the tip capacitance $C_{tip}$. An image charge is created by applying an voltage to the sample, with the tip grounded, through a charge amplifier. By oscillating the sample to tip voltage $V_{ac}$, one can shrink and expand the sample region occupied by the image charge, and locally measure transport characteristics by reading out the induced charge $Q_{ac}$ on the tip. High charge sensitivity can be achieved by locating it next to the tip inside the cooled AFM. This approach is simple, but can be very effective.
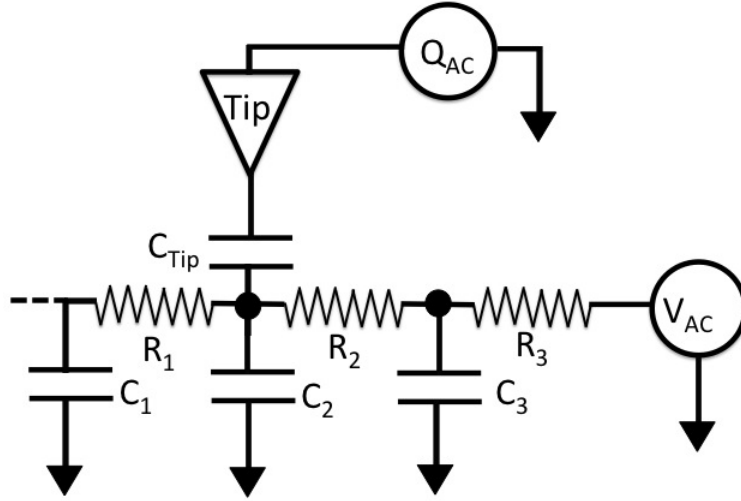


Figure 2.6: Scanning Capacitance Microscopy of a graphene channel is modeled by the circuit above. The tip-sample capacitance is denoted as ($C_{tip}$). The graphene channel can be modeled as series of resistors R1, R2 and R3 with local capacitances to ground $C_1$, $C_2$ and $C_3$. An AC voltage ($V_{AC}$) is applied to the 2DEG while the charge induced at the tip ($Q_{AC}$) is measured using the cooled preamplifier [36].

The SCM technique can also be used to map the geometric and quantum capacitance of a sample. The geometric capacitance is the electrostatic capacitance

determined by the sample geometry and dielectric constant. The quantum capacitance is associated with changes in the chemical potential of the material as quantum states are filled or emptied. For a semiconductor with a finite density of states dn/dE, the quantum capacitance is given by

$$\frac{1}{C_{total}} = \frac{1}{C_g} + \frac{1}{e^2 A dn/dE} \qquad (2.2)$$

where A is the capacitor area and e is the electronic charge. By measuring the quantum capacitance, SCM can map the density of quantum state in a nanoscale sample.

Another possible application of SCM is to individually tune isolated quantum dots in the Coulomb blockade regime even though the dot may have only one lead. A dc voltage applied between the contact(s) of the dot and the tip allows the tip to act as a movable gate that tunes the number of electrons on the dot. The dot conductance is measured at the same time by superimposing an ac sample-tip voltage and recording the resulting image charge via the tip's charge amplifier. This technique, used by Ashoori[37] and others promises to provide ways to probe very small dots under conditions where tunnel leads cannot be fabricated.

# Chapter 3

# Cooled Scanning Probe Microscope Apparatus

In this chapter, we discuss the improvements in the cooled scanning probe microscope apparatus that I carried out in the Westervelt lab. The ability to electrically and mechanically manipulate the microscope and sample at liquid He temperatures is critical for planned experiments to image the flow of electrons in graphene and other nanostructures. The objective of the improvements made in the microscope was to facilitate the positioning of tip and sample at helium temperature.

An illustration of the microscope is shown in Figure 3.1 in Mark Topinka's PhD thesis [38]. The microscope assembly consists of a head assembly where the tip is attached while the sample sits on top of a piezotube which is enclosed in a cage assembly. A typical scan is performed by translating the piezotube relative to the tip.

This chapter is divided into two main sections, the first of which, Section 3.1,

discusses the design and implementation of the head assembly, cage assembly, and feedthroughs. Section 3.4 covers connections from the microscope to other hardware, including sample, cantilever and piezotube control leads.
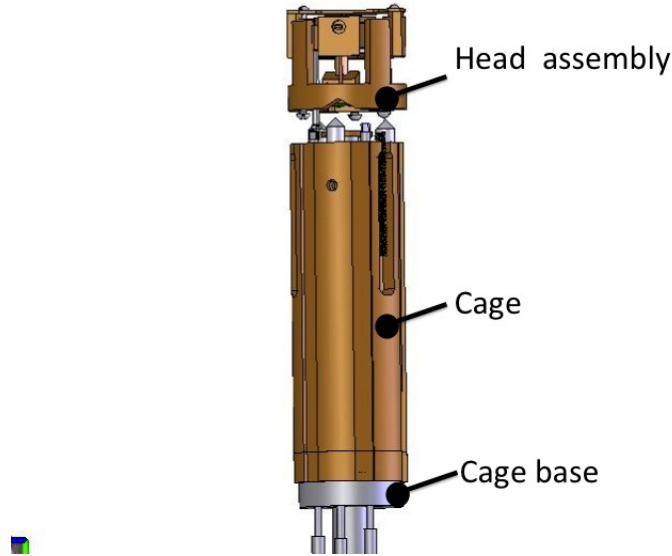


Figure 3.1: Illustration of microscope assembly noting the major components. Head assembly, cage assembly and the feedthroughs constitute the microscope. All the parts are made using brass for low thermal coefficient. The head assembly holds the tip, cage assembly houses the piezotube and allows access to the coarse positioning feedthroughs

## 3.1   Head assembly

The head assembly of the microscope consists of three major components - upper head, lower head and tip holder. As shown in Figure 3.2, the upper head is attached to the lower head via the three phosphor bronze posts. These phosphor bronze posts serve as a spring so that the upper head can be displaced relative to the lower head. This would be critical for the coarse positioning system which will be described in section 3.3.
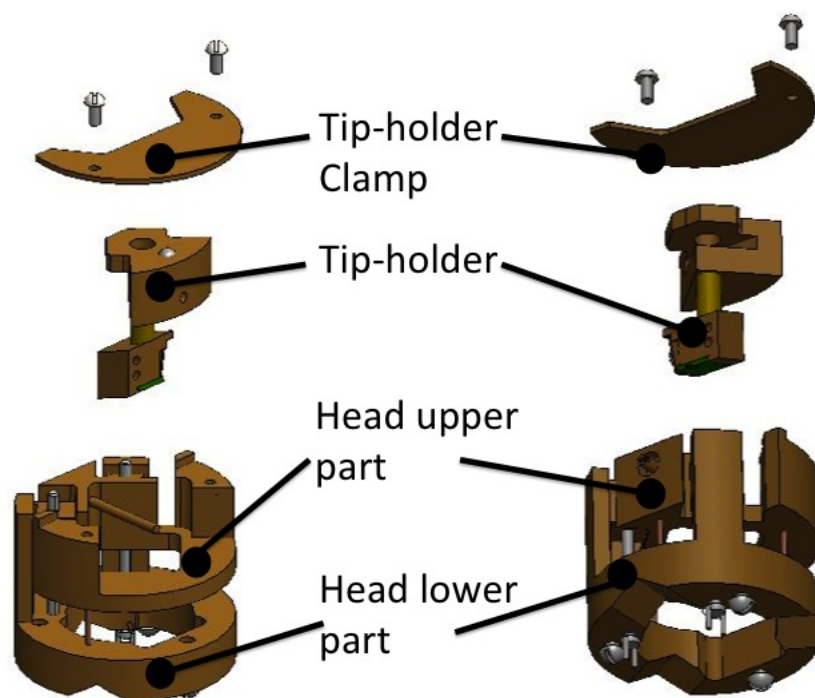
Figure 3.2: Exploded view of the head assembly. A clamp is screwed on top of the assembly that holds the tip holder in place. The tip holder has a press fit ball bearing on top and gets clamped on top of the upper head.

The head assembly has spring posts connecting the lower head to the upper head. The lower head sits on top of the three screws on the cage assembly and hence, the three V grooves where the screws are positioned. The three 2-56 holes on the bottom of lower head hosts three screw hooks for spring attachment to the cage assembly.
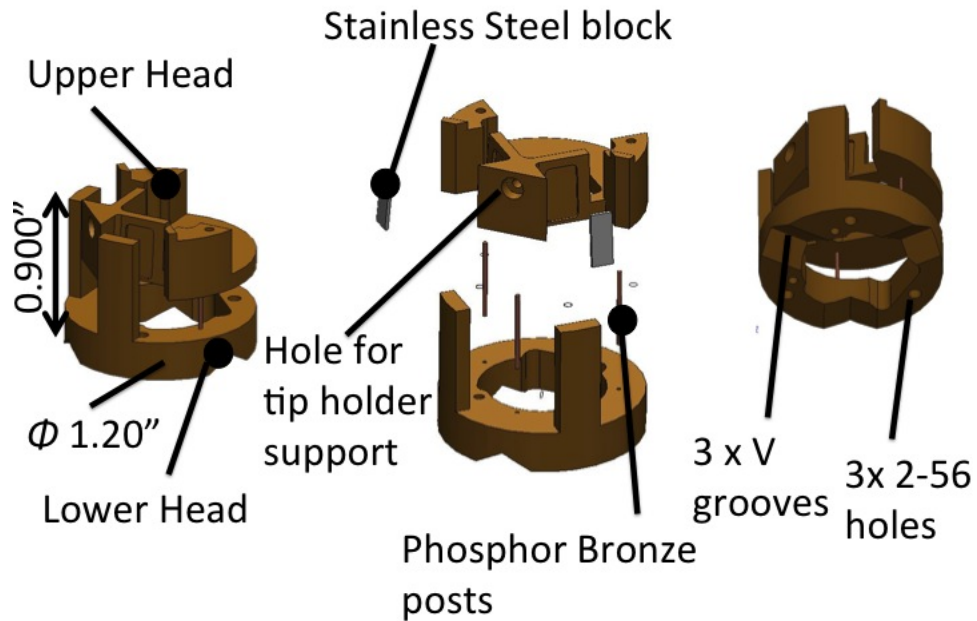
Figure 3.3: The left and right figures show the top and bottom views of lower and upper head while the center figure shows the exploded view of the upper and lower head.The head assembly is 0.9 inches tall and has circular width with a diameter of 0.12 inches. The upper head and lower head are attached to each other via the three phosphor bronze posts.There are three V grooves on the bottom side of the lower head such that it can be positioned on top of three screws coming from the cage assembly. There are three 2-56 threaded holes for screw hooks for spring attachment onto the cage. Solidworks File: newhead_1.sldasm

The coarse positioning system relies on the vertical motion of two wedges. The wedge pieces slide against the upper head forcing it to move sideways relative to lower head. This results in an in-plane movement of the tip holder which is clamped onto the upper head. The vertical motion of two wedges is achieved by turning two screws. As shown in Figure 3.4, the screws have long prongs that facilitate the contact with the flat head driver for low temperature coarse positioning.
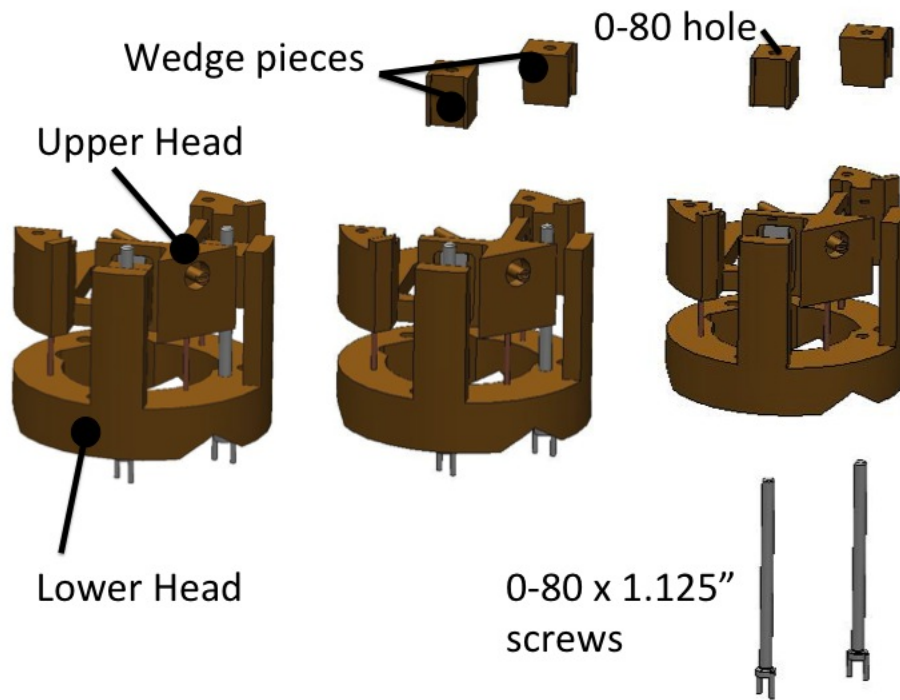
Figure 3.4: The coarse positioning system comprises of two 0-80 x 1.25" screws that can be driven by xy feed throughs. Each of the screws is screwed into the wedge piece. The wedges pieces move vertically when the screw is turned. This vertical movement translates to horizontal movement of the upper head. The screws are machined to have long prongs so that the flat head driver has enough contact at helium temperature even after thermal contraction.

Figure 3.5 shows the cross section of the upper and lower head which makes the coarse positioning mechanism clear. The opposite faces of wedge pieces have an angle of 5 degrees. This slope allows for the translation of the vertical movement of wedges into horizontal movement of the upper head. A ball bearing is press fit on the wedge such that contact area against the stainless steel block is minimized to achieve minimum amount of friction when performing the coarse positioning. Also, the stainless steel block is used instead of just brass to prevent wearing of the upper head over time from the sliding of ball bearing against the upper head.
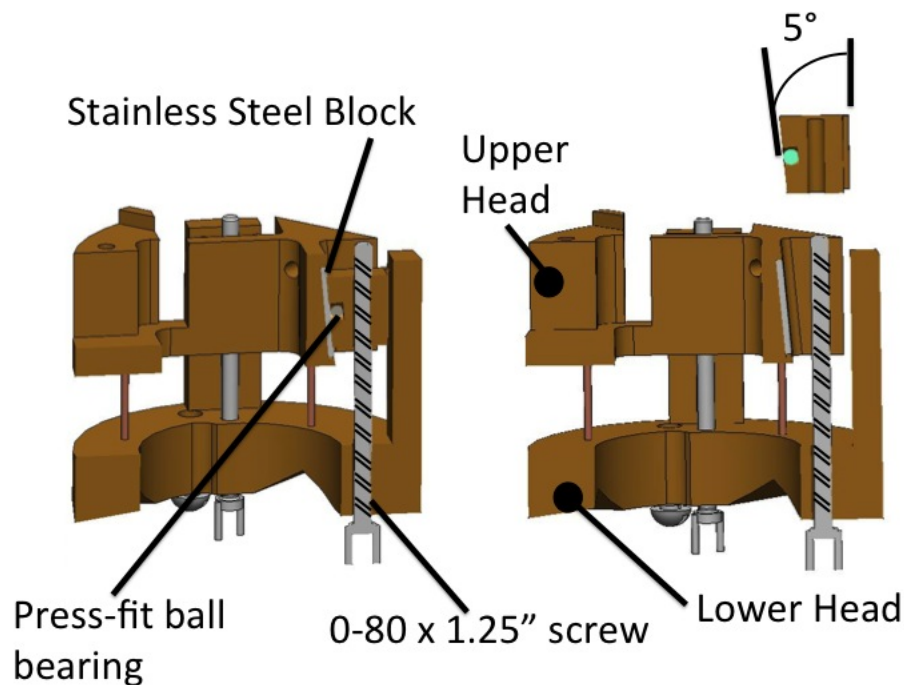
Figure 3.5: The figures show the cross section views of the lower and upper head. The 0-80 x 1.25" screw is turned clockwise or counter clock wise to push or pull the wedge piece that slides against the stainless steel block sitting on the groove on the upper head. The sliding of wedge piece against the stainless steel block forces the upper head to move sideways relative to the lower head. The angle between the two opposite sides of the wedge piece is 5 degrees. This slope allows us to convert the vertical movement to horizontal xy movement of the tip. Solidworks File: newhead_1.sldasm

## 3.2   Tip Holder

The tip holder consists of three major components- slider, support rod and clamp that holds the tip carrier chip. The slider is the top part of the tip holder which has a press-fit ball ball bearing so that it can slid on top the upper head for room temperature alignment. The slider also has a 0.14" through hole so it can be screwed onto the clamp at the bottom. The support rod's sole purpose is to keep the tip

holder from falling while performing room temperature alignment.
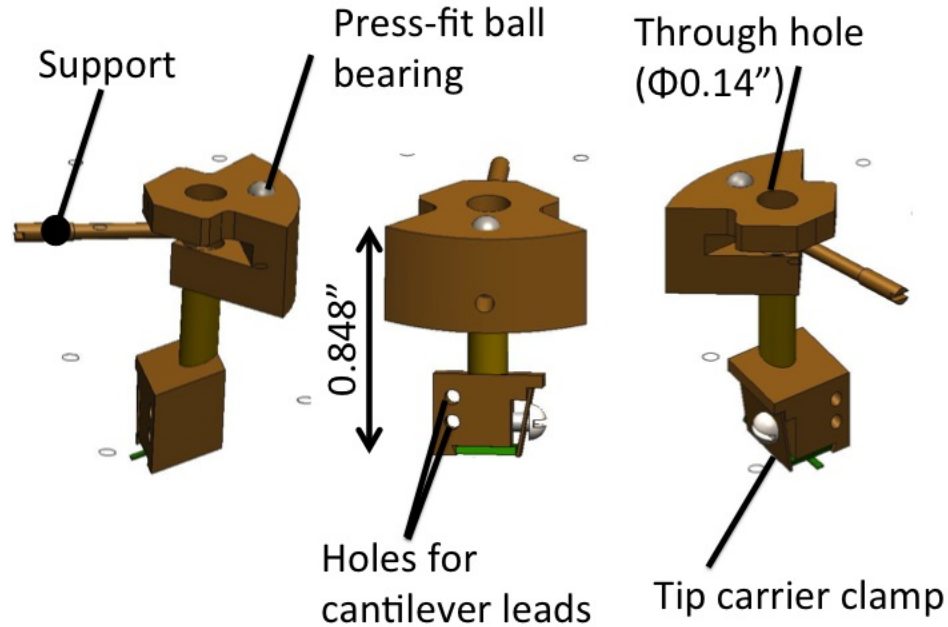


Figure 3.6: Illustration of the tip holder at different angles. There are three major components of the tip holder-slider, support and the clamp. Slider is the top part that consists of ball bearing on top and sits on top of the upper head. This is screwed onto the clamp (bottom end of the tip holder) via the 0.14" through hole. The support is a brass rod that is screwed onto the upper head and it's solely used to keep the tip holder from falling during room temperature alignment. The clamp holds the tip carrier chip and has two through holes for the cantilever leads. Solidworks File: tip holder.sldasm

In order for the coarse positioning technique to work properly, the tip holder needs to be designed such that tip inclination is around 20 degrees. This would ensure that the xy coarse positioning screws in the head assembly are aligned to the xy feedthroughs keeping the tip approximately vertical to the sample.
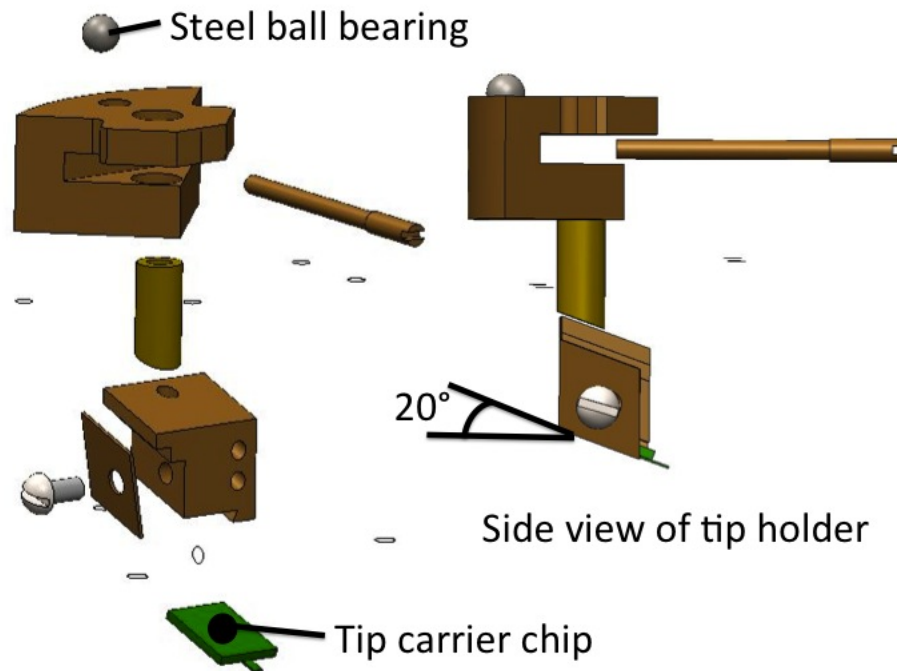
Figure 3.7: The left figure shows the different components separately that constitute the tip holder. The right figure shows tip holder from the side illustrating that the angle of the cantilever chip with slider is 20 degrees. Solidworks File: tip holder.sldasm

As shown in Figure 3.7, the tip holder is tilted to the horizontal plane for the coarse positioning system to work smoothly and it would also prevent the glue that sticks out of the tip carrier chip from hitting the sample. See Figure 3.12.

## 3.3    Feedthroughs

We use three rotating feedthroughs to manipulate the $z$ and $xy$ coarse positioning of the microscope. Electrical feedthroughs provide connection to the cantilever bridge, 12 sample leads, and five piezotube high voltage lines.
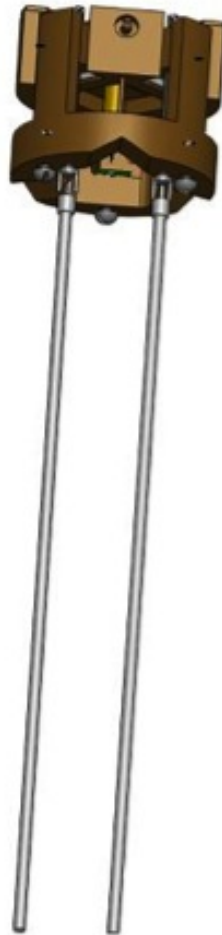
Figure 3.8: Illustration of the xy coarse positioning mechanism with head assembly. There are two xy feedthroughs with a flat head screw driver at the end that turn the xy positioning screws described in section 3.1. Solidworks File: everything.sldasm

Figure 3.8 illustrates the rotating feedthrough mechanism that allows us to perform coarse positioning along xy direction of the sample at helium temperature. The head assembly consists of the head and the cantilever chip carrier. The flat head driver turns the screws that move the wedge as mentioned in section 3.1.
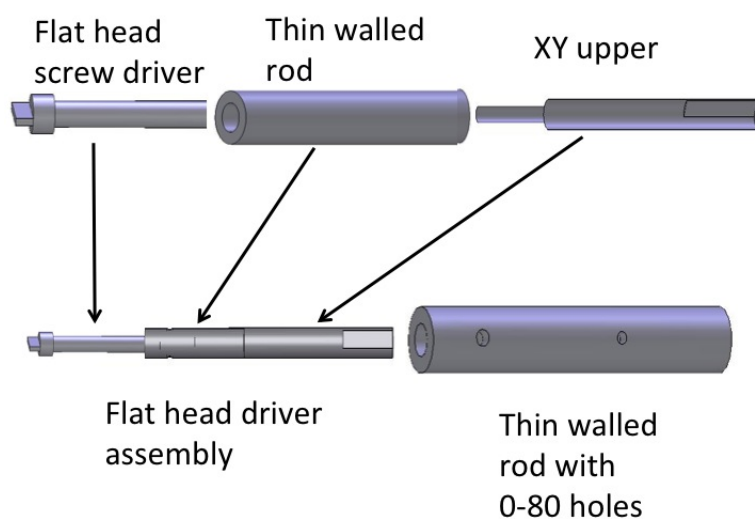
Figure 3.9: Illustration of the xy feedthroughs. The xy feedthroughs have three components - flat head driver, 0.1" thin walled stainless steel rod and xy upper. All these parts are epoxied together to form the xy feedthrough at the lower end of the insert.

As shown in Figure 3.9, the feedthroughs have three major components- flat head screw driver, thin walled stainless steel rod and the xy upper. The parts are epoxied together. The use of thin walled stainless steel rod helps to reduce the thermal conduction along the feedthroughs.
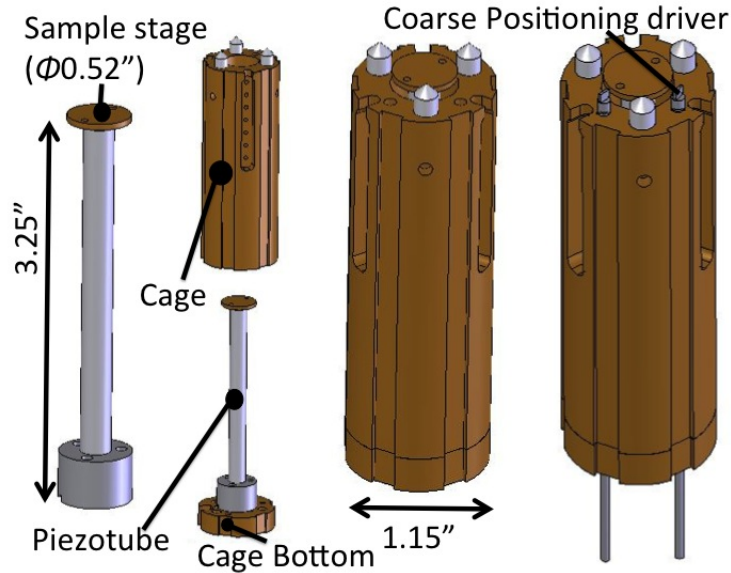
Figure 3.10: The leftmost figure shows the piezotube with sample stage on top and a macor piece on the bottom. The next figure shows the piezotube on top of a cage base. Adding the piezotube onto the cage makes the cage assembly shown in the next figure. The rightmost figure shows two coarse positioning feedthroughs in the cage assembly. The holes are designed to fit the coarse positioning feedthroughs such that they are alined to screws on the head assembly. Solidworks File:new_microscope.sldasm

Two vertical feedthrough rods, shown in Figure 3.2, provide access to the $xy$ coarse positioning screws of the microscope head. Each rod is comprised of a length of 0.1" diameter thin walled stainless steel with stainless steel caps epoxied to each end. The lower cap ends in a flat head driver accepted by the coarse positioning screw while the upper ends to the double joint rods in the top part of the insert.

Figure 3.11 illustrates the rotating feedthrough assembly implemented in the microscope. Mechanical access to the coldspace is achieved through the use of three Ferrotech rotating vacuum feedthroughs (model SS-188-SLAA). The rotation from the feedthroughs is transferred to the xy coarse positioning rods and z approach rod through two double joints as shown in Figure 3.11 that attaches directly to the vac-

uum feedthrough. Much of the feedthroughs are made up of thin walled stainless steel which provides high thermal impedance between the room temperature feedthrough and the coldspace.
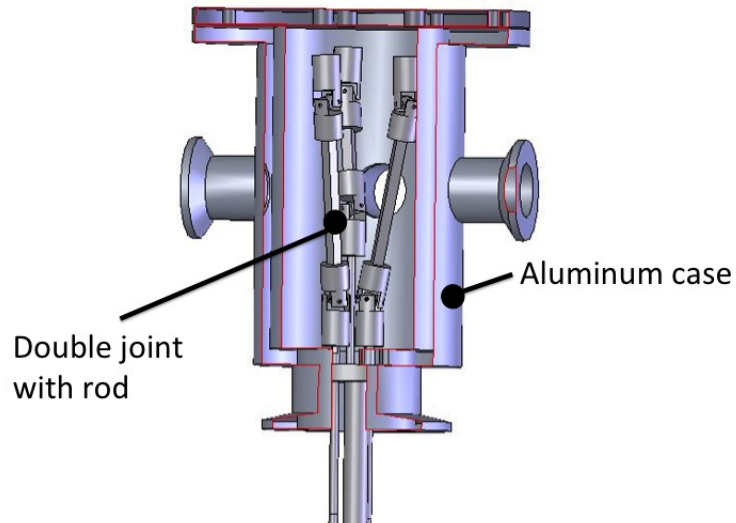


Figure 3.11: Illustration of the double joint mechanism on the top end of the insert that transfers the mechanical motion from the xy and z feedthroughs into the sample coldspace.

**Z Coarse Approach**

The $z$ coarse approach is the third vertical feedthrough rod which provides access to the $z$ coarse approach ball end screw. This rod is also constructed from three parts similar to that of the $xy$ coarse positioning feedthrough rods. The upper end is attached to a gear mechanism that reduces the rotation by a ratio of 16:1. The lower end of the feedthrough is a 1.5 mm hex accepted by the $z$ coarse approach ball end screw.

### 3.3.1 Electrical Feedthroughs

Appropriate material needs to be chosen for the conducting wires used for the sample leads and high voltage lines because as determined by the Wiedemann-Franz law, the thermal conductivity, $\kappa$, and electrical conductivity, $\sigma$, of a metal are related by,

$$\kappa = L_o \sigma T, \tag{3.1}$$

where $T$ is the temperature of the material and $L_o$ is Lorenz number with a value $2.443 \times 10^{-8} W\Omega/K^2$. This suggests that the high resistance wire would prevent less heat from getting into the coldspace from outside. Hence, high resistance materials such as fine gauge manganin wire and stainless steel are used for all the electrical feedthroughs.

**Sample Leads and Cantilever Bridge Leads**

Sixteen sample leads enter the cryostat through a 16-pin Fischer connector (DBEE 104 A086). Similarly, four leads for the cantilever bridge circuit and two leads for the silicon temperature sensor enter through another 11-pin Fischer connector. AWG 32 manganin (a copper, manganese, nickel alloy) wire is used for all the connections as it provides a high resistance electrical connection into the coldspace.

### 3.3.2 Cantilever tip

We use a piezoresistive cantilever tip for our SPM. The tip radius is 20 nm. The deflection of the cantilever is measured by recording the piezoresistance using a bridge

circuit very close to the cantilever in the cryostat. The output of the bridge circuit is then amplified further by two room temperature amplifiers.
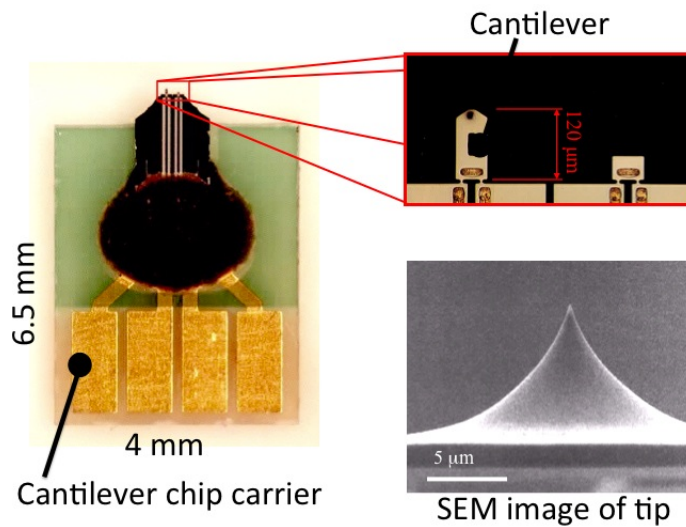


Figure 3.12: The left figure shows the cantilever chip carrier with the soldering pads. The black circular object at the center of the chip carrier is epoxy that holds together the cantilever leads. The top right figure shows the cantilever which is 120 um long and the small speck on the top end of the cantilever is the tip. The bottom right figure shows the SEM image of tip.

## High Voltage Leads

The High voltage leads for driving the piezotube enter the cryostat through a 6-pin Fischer connector (DBEE 104 A065). These high voltages lines are ultra miniature stainless steel coaxial cables produced by Lakeshore Cryotronics, of Westerville, OH in order to reduce the pickup in the sample measurement leads and also to reduce the thermal conduction from room temperature to helium temperature.

## 3.4 Other connections to Cryostat

### 3.4.1 SPM electronics

The electronics for SPM include the feedback controller, xy voltage controller for scanning and DAC for generating required voltages for the transport measurement. The software and the electronics for the SPM was designed by Katherine Aidala. The details of design and operation of the electronics for SPM are in Aidala's thesis [39].

### 3.4.2 Sample Lead Breakout box

The access to the sample leads is provided by a breakout box which connects directly to the sample lead Fischer connector. The breakout box contains 13 BNC plugs where 12 provide connections to the sample leads in the coldspace while one provides access to the cryostat ground. This ground is simply connected to rack ground which is a common ground for all the electronics.

# Chapter 4

# Cooled Scanning Capacitance Microscope

## 4.1 Introduction

Scanning probe techniques have been of great significance in studying local electronic behavior of a two dimensional electron gas (2DEG) in materials such as graphene [23] and GaAs/Al$_3$Ga$_7$As heterostructures [2, 37, 40]. In these techniques, images of local electron flow were obtained by having a very narrow (20 nm to 200 nm) charged AFM tip scanned or positioned directly above the 2DEG while the conductance through the sample [2, 23, 32], or the capacitance between the sample and tip, is measured [37, 40]. The scanned capacitance microscope technique uses a sharp metal tip, which is held above the 2DEG surface and is capacitively coupled to the 2DEG immediately below [37, 40]. When a small AC voltage is applied between the tip and the 2DEG, the resulting flow of charge in the gas induces an oscillating image charge

on the tip; that oscillation is detected by a sensitive electrometer. This technique can be very useful in mapping the local electron density. Ashoori's group[37, 40] used this technique to map the location of Landau levels of a 2DEG in the quantum Hall regime in a strong magnetic field at low temperatures.

This chapter begins in Section 4.2.3 with a description of the cryogen cooled preamplifier. Section 4.3.1 discusses the experimental results obtained from scanning capacitance microscopy.

## 4.2  Method

We have developed a scanning capacitance microscope to image the capacitance of a sample on a nanometer scale. As shown in Figure 4.1, the technique uses a metal tip scanned above the sample as the capacitance between the tip and sample is measured. To verify the operation of the instrument, it was tested on a sample that consists of a 15 nm thick gold electrode deposited on a Si/SiO$_2$ substrate, shown in the inset to Figure 4.1. The tip was scanned across the edge of this gold electrode so that corresponding change of capacitance can be measured. In addition, another experiment was done where a tip of radius 2.5 um was used to verify the operation of the constructed scanning capacitance micrsocope. In this experiment, the distance between the tip and sample is varied while the change in capacitance is recorded.
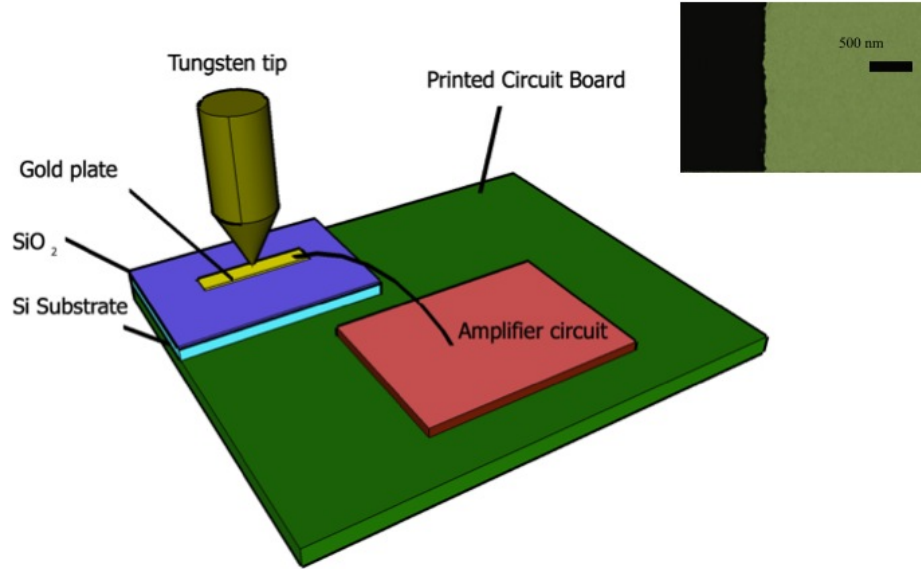
Figure 4.1: Schematic of scanning capacitance microscope experimental apparatus. Tungsten tip of diameter 1 um is scanned at 20 nm above a 15 nm gold plate deposited on top of a $SiO_2$ substrate. The charge amplifier circuit measures the change in capacitance as the tip is scanned. Both the sample and circuit are mounted on a printed circuit board. The inset on the top right shows the scanning electron microsope image of the gold electrode.

## 4.2.1    Charge amplifier

The charge sensing circuit shown in Figure 4.2 uses a capacitance bridge circuit followed by a two-stage common base amplifier circuit. Because the experiments need to be performed at low temperatures to observe quantum mechanical effects, we use high electron mobility transistors (HEMT) for the amplifier circuit. We chose a low noise (0.55 dB @ f = 12 GHz) pHEMT for this purpose.
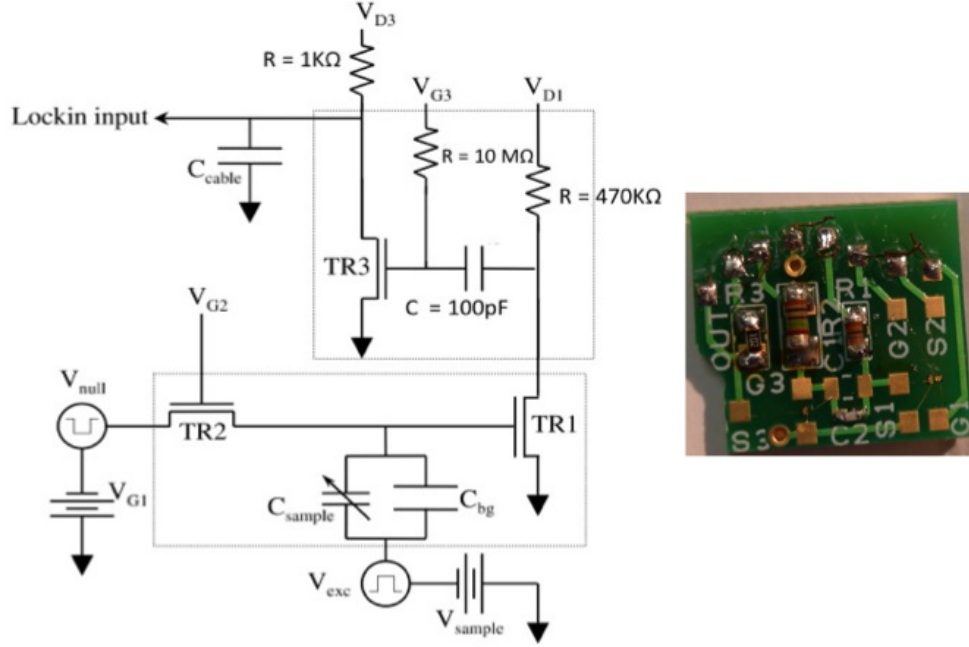
Figure 4.2: Left image is the schematic of pre-amplifier circuit. TR1, TR2 and TR3 are high electron mobility transistors(HEMT). The circuit is a capacitance bridge formed by tip-sample capacitance and a reference capacitor followed by at two stage common base amplifiers. The right image is the picture of the circuit on a printed circuit board[37].

As shown in Figure 4.2, the capacitance between the tip and sample can be modeled as $C_{samp}$. The transistors TR1, TR2 and TR3 are HEMTs in our circuit. We use TR2 as a reference capacitor by pinching it off as a pinch voltage is applied in $V_{G2}$. The nominal source-drain capacitance for the transistor is 150 fF. As a typical capacitance bridge circuit, an ac voltage VS1 is applied to the sample while a second ac voltage VR1 is applied to the reference capacitor. The sample voltage VR1 is adjusted (both phase and amplitude) such that the voltage at junction node of reference capacitor and sample capacitor is zero. This means that the bridge is balanced

and any change in the sample-tip capacitance would bring the bridge off balance and hence a change in voltage at the node.

The two-stage common base amplifier circuit amplifies the small change in voltage. The first stage consists of TR1 and a resistor R = 470 k. The value of the resistor was chosen in order to achieve maximum gain at our first stage. The transistor in this stage is operated at saturation point again to maximize gain. The second stage consists of TR 3 and a resistor R = 1kΩ. The transistor TR3 is biased at triode region to allow maximum current so that its enough to drive the long cables coming out of the cryostat to the lock-in amplifier that sits outside the cryostat. The estimated impedance in the cables is about 5 k and hence we set out output impedance of the amplifier to about 2 k. The 100 pF capacitor that sits between the first stage and second stage amplifier allows us to bias the TR2 as it only allow ac coupling between first stage and second stage circuits. The operating frequency of our experiment is set to 210 kHz (maximum frequency possible in lock-in amplifier) to minimize the 1/f noise in our signal. The bypass capacitor with a value of 100 pF has a lower cut-off frequency of 1 kHz which minimizes attenuation of signal going from stage 1 to stage 2.

The dc voltages that bias the amplifier circuits were generated using a homemade low-noise, battery-operated dc source, shown in Figure 4.3. Two 6V batteries along with two low-noise (15.1 uV rms @ 100 kHz) adjustable output TPS7A30001 dc-dc converters were used. The output of the dc-dc converter was fed to a simple potential divider connected to a unity gain amplifier. Six different replicas of the circuit were made to create all the necessary biasing/gate voltages for the amplifier circuits.

## 4.2.2 DC/AC voltage supply
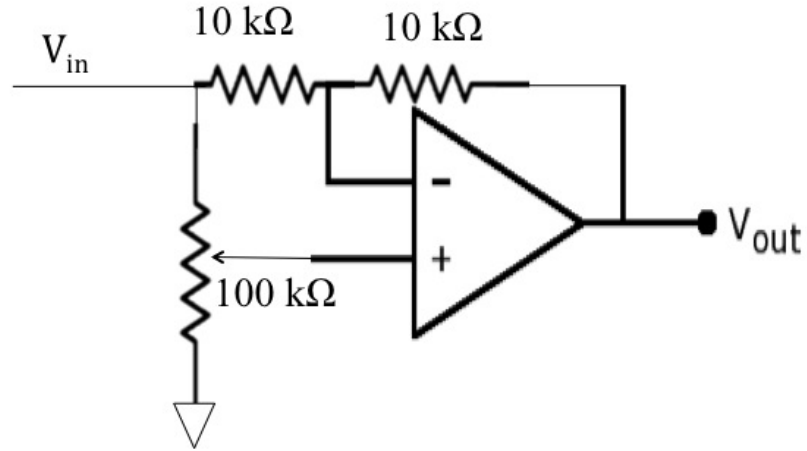


Figure 4.3: Schematic of the dc voltage supply to biasing transistors in the preamp. The circuit consists of dc-to-dc converter that generates 6 V, followed by a potentiometer and a unity gain amplifier.

The ac voltage source for the amplifier circuit was also homebuilt to achieve a low noise figure. It consists of two 6 V batteries which are connected to a dc-to-dc converter shown in Figure 4.4 to maintain a constant voltage supply. A Wien Bridge Oscillator (I) is used for generating a low-distortion sinusoidal wave. The components are selected such that the frequency is set to 200 kHz (f = 1/2RC). This is followed by a buffer amplifier (II) with unity gain to have low output impedance. A phase shifter (III) along with a potential divider (IV) is used for changing the phase and

amplitude of the sine wave. Two copies of this circuit are used to generate two ac signals with independently adjustable phase and amplitude needed for the capacitance bridge described earlier.

### 4.2.3   AC voltage source
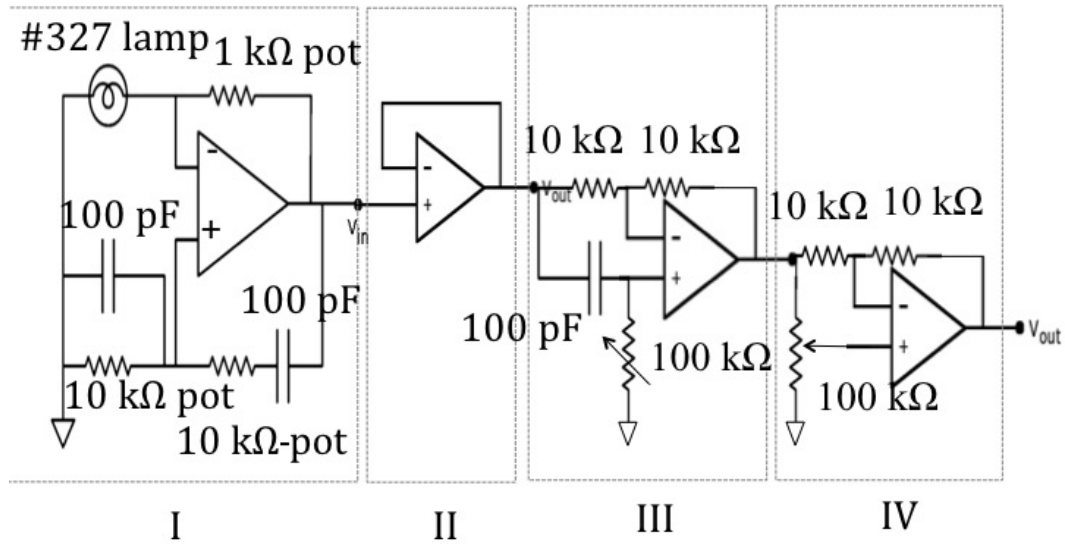


Figure 4.4: Schematic of variable phase and amplitude ac source. The dc-to-dc converter provides a constant power supply to the ac generator circuit. The ac generator circuit consists of four stages. Stage I is a Wien bridge oscillator, that generates sine wave of frequency 210 kHz followed by Stage II, a buffer amplifier. Stage III and IV consists of phase shifting circuit and a buffered potential divider respectively.

The dc voltage sources and ac voltage sources are put in separate enclosures to prevent ac interference in the dc source. These sources remain outside the cryostat

while the preamp operates at liquid helium temperature mounted right on the scanning probe microscope. All the cables that lead to and from the preamplifier circuit are low thermal conductivity coaxial cables. For the purpose of adding the dc voltage with the ac signal, a simple RC junction is used. The input voltage noise of the circuit was obtained by grounding both the input terminals and measuring the output voltage noise using a lock-in amplifier. The input noise measured at the temperature 4.2 K is $20nV/\sqrt{Hz}$. The stray capacitance of the preamp was measured to be 1 pF in reference to the input. The charge noise was obtained by the relation $\Delta Q = C\Delta V$ = $0.13e^-/\sqrt{Hz}$.

## 4.3   Experimental Results

The experimental results for the two-dimensional capacitance scan over the edge of gold electrode is shown in Figure 4.5. The change in capacitance of 30 aF is clearly visible and a step can be noticed right along the edge of the electrode.
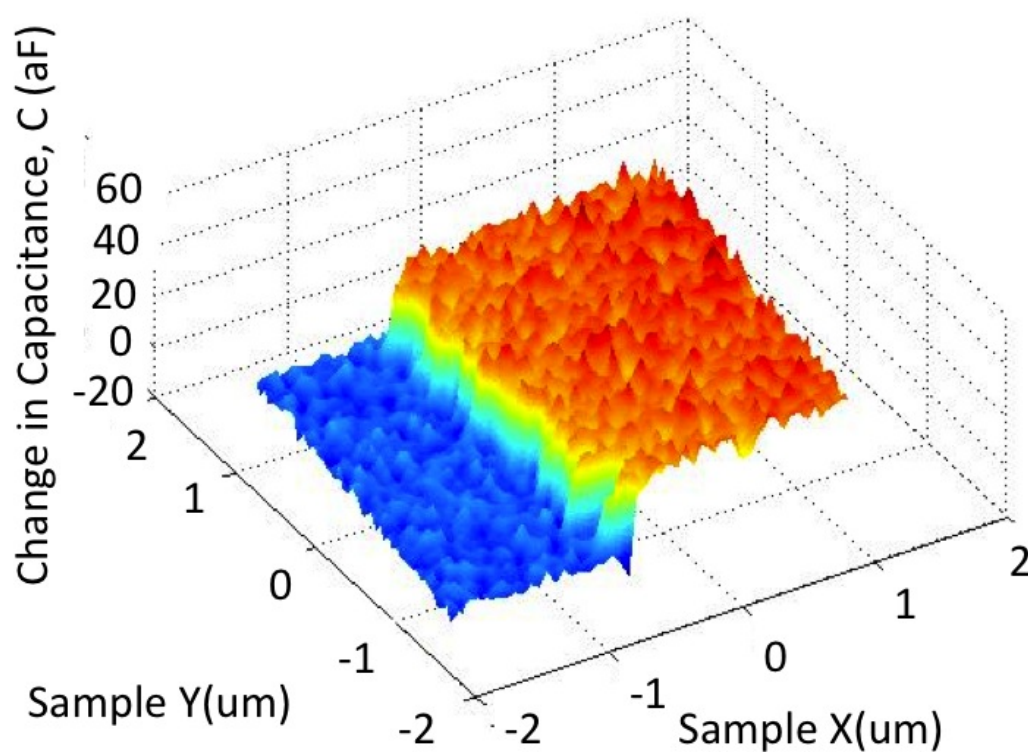
Figure 4.5: Capacitance-scan of the two-dimensional sample. The height of plot represents change in capacitance (aF) as the tip is scanned at a height of 20 nm on top of the edge of the 15 nm gold electrode. The change in capacitance is 30 aF.

To compute the spatial resolution of our scanning capacitance setup, the capacitance measurements were averaged over a range $\Delta y = 0.30$ $\mu$m of the flat edge and plotted vs. x in Figure 4.6. The total width of the transition is $\Delta x = 100$ nm.
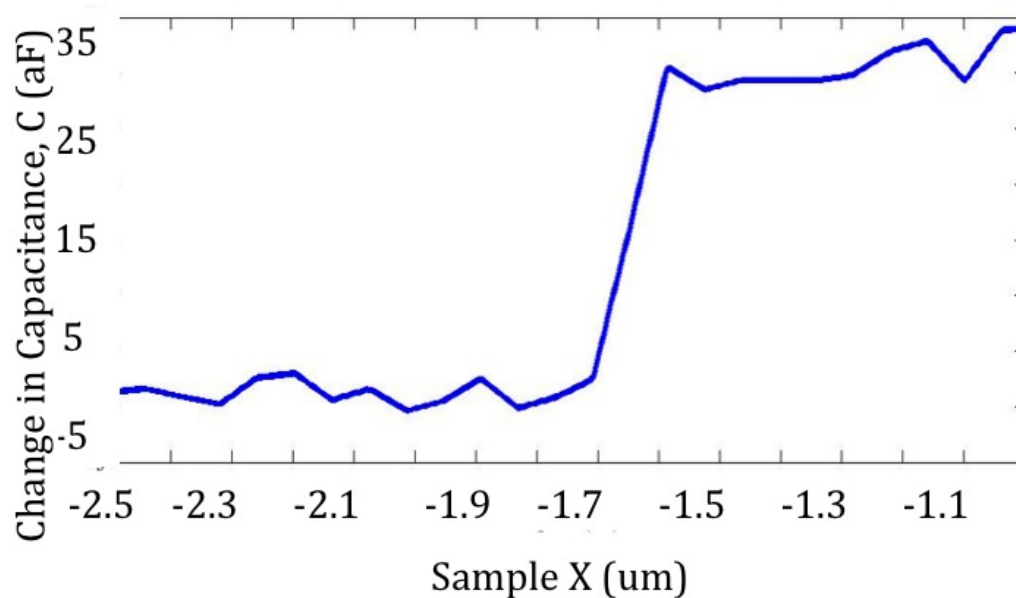
Figure 4.6: Capacitance change vs. tip x averaged between -0.2 $\mu$m < y < -0.5 $\mu$m as the tip is scanned across the edge of the gold electrode. The full spatial width of the capacitance transition is 100 nm.

The change in tip-sample capacitance as the tip is swept over the edge of the conducting sheet is determined by the tip-sample distance. Figure 4.7 shows the tip-sample capacitance measured for 2.5 um radius tip as the tip-sample distance is varied, along with COMSOL simulations of the capacitance between a conducting sphere of the same radius and a conducting plate. As shown, the theoretical and experimental results agree quite well for tip-sample distances less than 200 nm.
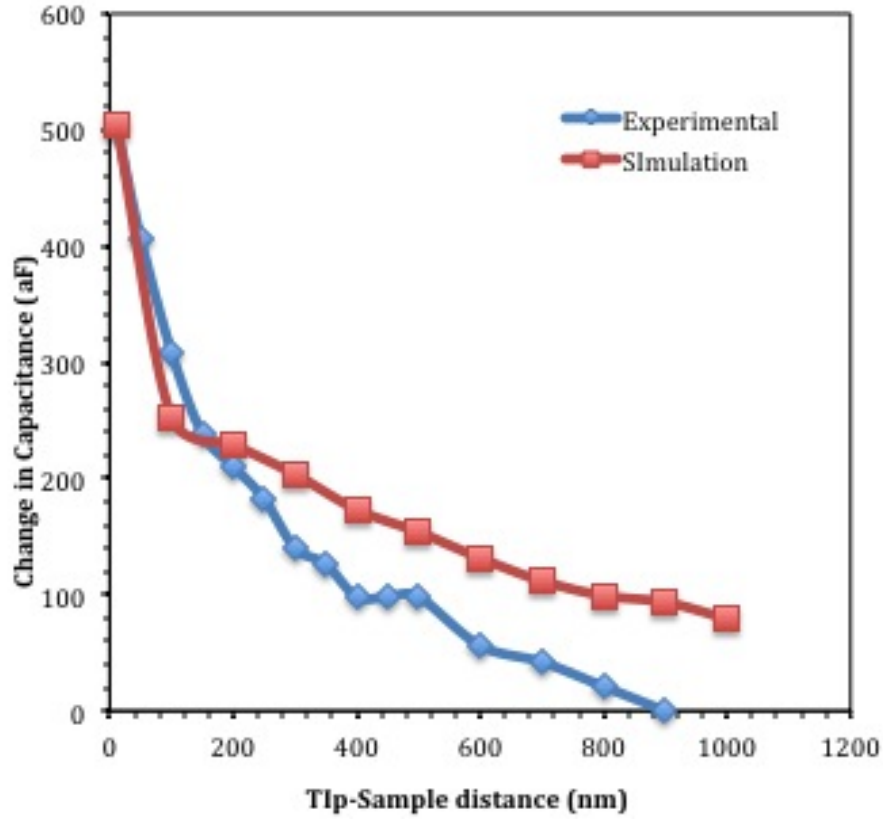
Figure 4.7: The tip-sample capacitance is plotted vs. tip-sample distance. The red curve shows COMSOL simulations while the blue is the experimental result. A tip with diameter 5 um was used.

### 4.3.1 Theory and Simulation

To analyze the capacitive image of the conducting plate edge shown in Figure 4.5 and Figure 4.6, we used COMSOL to simulate the tip-sample conductance between a conducting sphere and a conducting plate shown in Figure 4.8. The simulation geometry is shown on the left, where a metal sphere (reddish brown) is located at a distance of 20 nm above a conducting plate (reddish brown), on top of a $SiO_2$ layer (grey). The right side of Figure 4.8 shows the image charge in the conducting plate,

represented by the normal component of electric field at the plate's surface in the simulations. As seen in Figure 4.8, the FWHM of the image charge induced by the voltage on the tip is 210 nm, which gives a spatial resolution of the half width at half maximum HWHM 105 nm. This agrees with the experimental results of the scanning capacitance over the electrode edge.
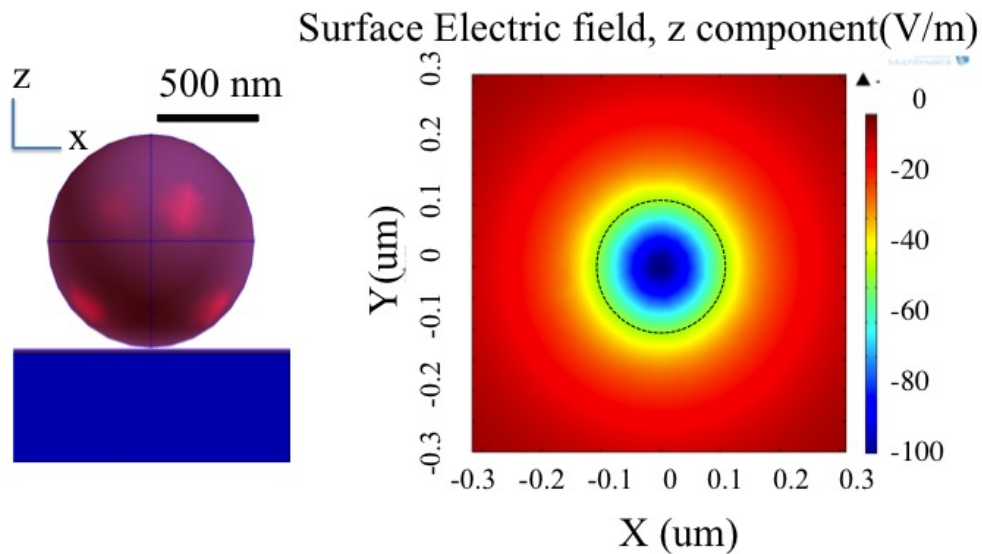


Figure 4.8: (left) Geometry for COMSOL simulations showing the tip (modelled as a conducting sphere) positioned at a height of 20 nm above a conducting metal plate (reddish brown) sitting on a SiO$_2$ substrate (grey). (right) Normal electric field on the metal plate surface, proportional to the image charge density. The FWHM from the dashed line fit is 210 nm, which predicts a spatial resolution 100 nm in the experiments shown in Figure 3.5 and 3.6, in agreement with the data.

The agreement between the experimental results and simulation suggests that the technique can image local capacitance with a spatial resolution 100 nm when the scan

is performed at with the tip 20 nm above the sample surface, with a tip diameter of $1\mu$m. The noise level of the preamp circuit is $0.1\mathrm{e}^{-}/\sqrt{Hz}$. Future experiments using this setup would be to image electronic density profile in graphene edges or quantum dots [5]. It could equally be used to obtain a high-resolution two-dimensional image of local capacitance change in other materials.

# Chapter 5

# Imaging magnetic focusing of electrons in graphene

## 5.1  Introduction

Using hexagonal boron nitride (hBN) as a substrate greatly enhances the mobility of electrons in graphene samples. As a result, electrons in graphene can travel several microns without scattering at low temperatures and follow classical trajectories as their motion becomes ballistic. When a magnetic field is applied perpendicular to the plane, electrons follow cyclotron orbits, as one would expect classically. Magnetic focusing occurs for electrons travelling from one point contact to another in a perpendicular magnetic field B, when the spacing between the two point contacts is an integer multiple of the cyclotron diameter $2r_c$. Electrons entering the graphene sample at different angles all follow circular trajectories - as a consequence of this geometry, the electron flux peaks at a distance $2r_c$. As B is increased from zero, the

electron transmission from one point contact to the other peaks when their separation L is equal to the cyclotron diameter $2r_c$. As the field continues to increase additional peaks occur when the separation L is an integer multiple of the cyclotron diameter $2nr_c$, because the electron orbit skips along the edge [41]. In this chapter we present images of electron cyclotron orbits in graphene, associated with magnetic focusing, which were recorded using a cooled scanning gate microscope [14, 2, 6].

In the scanning gate technique, the conducting tip of a scanned probe microscope is held just above the sample surface, and an applied tip-to-sample voltage creates an image charge that is moved while the transmission between two point contacts is measured. The magnetic focusing of a two-dimensional electron gas (2DEG) in GaAs/AlGaAs heterostructures [6] has been imaged using this technique. In this chapter, we report imaging of magnetic focusing of electrons in graphene at 4.7 K. The sample is a high mobility hBN-graphene-hBN sandwich etched into hall bar geometry shown in Figure 5.1. By tuning the transverse magnetic field B and electron density n in the graphene layer, we observe the first magnetic focusing peaks. For values of B and n on first magnetic focusing peak, we observe an image of the cyclotron orbit that extends from one point contact to the other. We also study the effects of B and n on the spatial distribution of electron trajectories.

## 5.2   Experimental setup
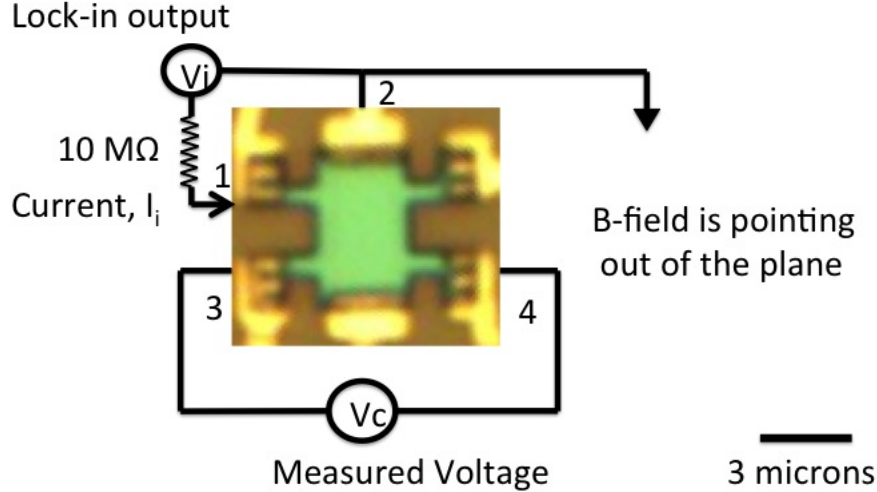


Figure 5.1: The sample is a hBN-graphene-hBN structure etched into a hall bar geometry. For the magnetic focusing measurement, point contact labeled as "1" is where the current is injected into graphene. An ac current $I_i = 1.0$ $\mu$m at 5 kHz is injected between point contact 1 and the grounded end contact 2. Point contact 2 is connected to ground while the voltage difference between point contact 2 and 4 ($V_c$) is measured using the lockin amplifier. The degree of focusing is measured by the transresistance, $R_m = V_c/I_i$. We use a cooled scanning gate microscope [14, 2, 6] to image such cyclotron trajectories in graphene.

Figure 5.1 is an optical image of a Hall bar sample constructed from a hBN/graphene/hBN

sandwich assembled in Philip Kim's lab at Harvard. The Hall bar has dimensions

3.0 $\mu$m $\times$ 4.0 $\mu$m, with two point contacts separated by 0.7 $\mu$m on either side and

large contacts at either end. The substrate is an 285 nm layer of $SiO_2$ on a heavilty

doped Si substrate that acts as a backgate. The backgate capacitance is $C_g = 1.15$

$\times$ $10^{-8}$ F. The density can be tuned to be either electrons or holes by applying an

appropriate voltage $V_{gate}$ between the backgate and the sample. The charge density n in the graphene is:

$$n = (V_{gate} - V_{dirac}) \times C_g/e \tag{5.1}$$

where e is the elementary charge and and $V_{diary}$ is the backgate voltage that nulls the electron density, and puts the Fermi level at the Dirac point.

To carry out the magnetic focusing measurements, a current source injects a current that flows from the point contact 2 to the wide end contact 1 in Figure 5.1. Magnetic focusing is sensed by measuring the voltage between point contacts 3 and 4 in Figure 5.1. Electrons entering at point contact 2 flow in a clockwise direction along cyclotron orbits in the graphene and arrive at point contact 3. No current can flow through that contact, so its chemical potential increases until a reverse current is created that cancels the arriving current, via the principle of detailed balance. The increase in chemical potential is measured by the voltage Vc between point contacts 3 and 4, and the magnetic focusing signal is the transresistance $R_m = V_c/I_i$.

## 5.3   Results

To quantify the sample quality in terms of its electron mobility, we use a four probe measurement technique. A current $I_i$ is passed between the contacts 2 and 4, while the voltage $V_s$ is measured between point contacts 1 and 3. The measured resistance $R_s = V_s/I_i$ is plotted vs. the density n in Figure 5.2.
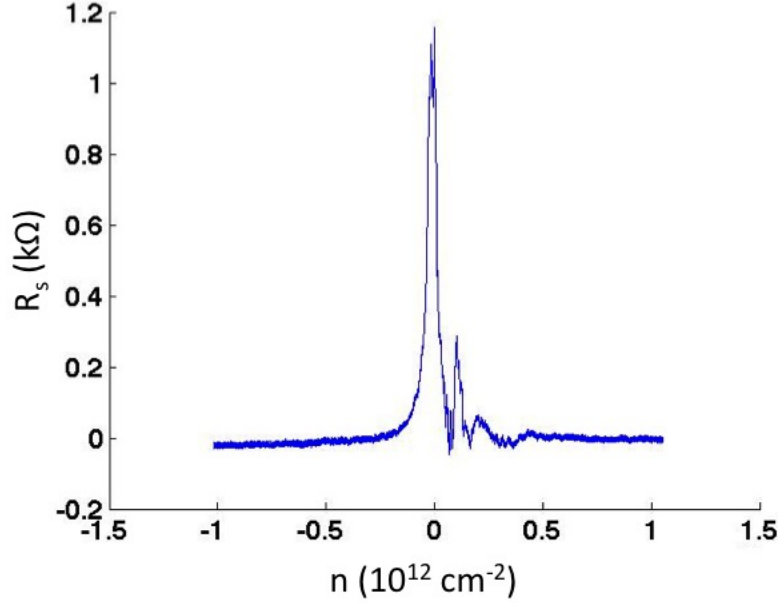
Figure 5.2: Plot of the 4-point resistance $R_s$ vs. electron density n at T = 4.7 K for the sample shown in Figure 5.1. The density is computed from the backgate voltage $V_{gate}$ and the gate capacitance $V_g$ using Equation 5.1. This four probe measurement shows a clear Dirac peak with electron mobility of $300,000 cm^2/Vs$ .

As shown in Figure 5.2, a sharp resistance peak is present at the dirac point where the nominal density goes to zero. At the density $n = 5$ x $10^{11}$ cm$^{-2}$, the mobility is $\mu = 200,000$ cm$^2$/Vs. The mean free path, $l$ of electrons can be computed using the relation.

$$l = \frac{h}{2e^2\rho\sqrt{\pi n}} \tag{5.2}$$

where $\rho$ is resistivity, h is Planck's constant, e is elementary charge and n is the density of charge carriers. Using this relation, the mean free path is estimated to be l = 1.7 um. The mean free path is in the same order of magnitude as the distance between the point contacts.

The first magnetic focusing peaks are shown in Figure 5.3, which is plot of the transresistance ($R_m$) vs electron density (n) and perpendicular magnetic field B at T = 4.7 K. The trans-resistance, $R_m$, is plotted as colormap vs magnetic field (B) and electron density (n). The color red represents the maximum in trans-resistance, $R_m$ while the color blue represents the minimum. The theoretically predicted value (Equation 2.1) for the first two magnetic focusing peaks .i.e., the peak in transresistance is represented by the dashed line.

There is slight deviation in the experimental value from theoretically predicted value for the magnetic focusing peak. The charge density peaks at the edge of the sample, due to fringing fields from the back gate which diverge at the atomic layer edge.
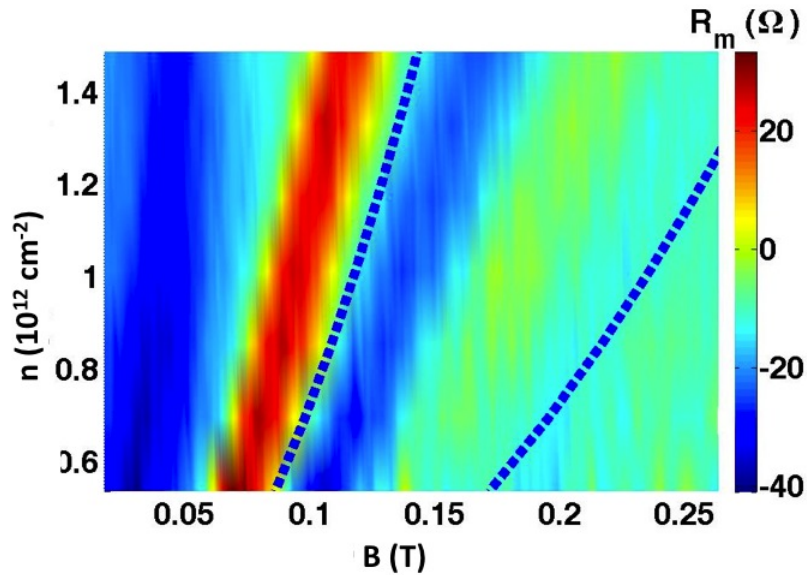


Figure 5.3: The transresistance $R_m$ vs magnetic field B and electron density n. The color red represents the maximum in trans-resistance $R_m$ while the color blue represents the minimum. The dashed lines represent the theoretically predicted value for the first two magnetic focusing peaks.

For the scanning gate measurement, a tip of 20 nm radius was brought at a distance of 10 nm above the BN surface (70 nm above graphene layer). The tip was raster scanned while simultaneously measuring trans-resistance. Figure 5.4 shows images of electron flow: the left figure shows the image when no magnetic field is applied to sample and hence, no magnetic focusing signal is seen. The right figure shows the image of cyclotron orbits of the electrons while the magnetic field and charge density were tuned to the first focusing peak in Figure 5.3 at density n $= 1.2 \times 10^{12}$ cm$^{-2}$ and magnetic field B $= 0.107$ T.
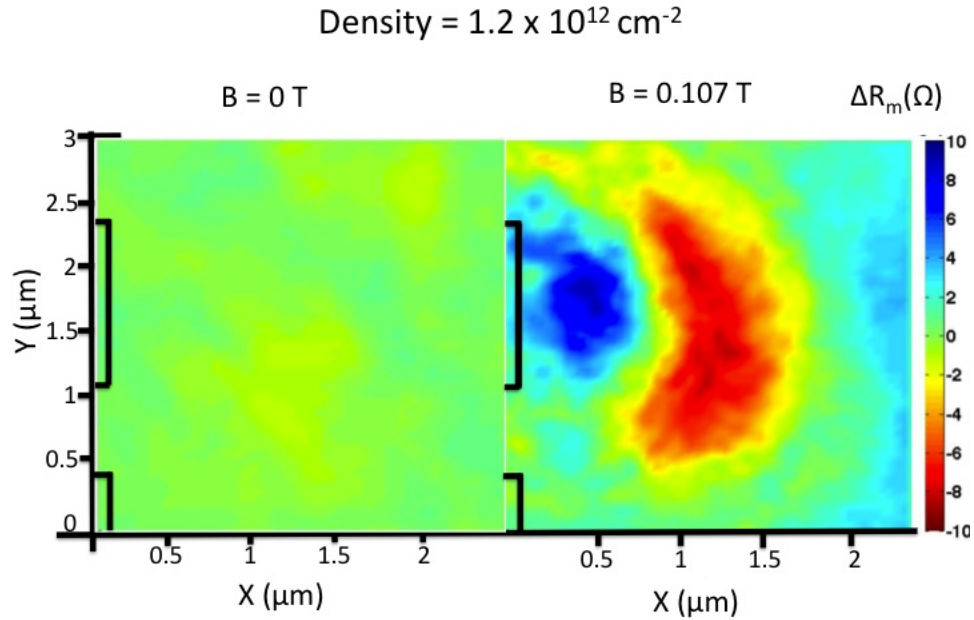


Figure 5.4: This figure shows the images of turning on and off the magnetic focusing respectively. The left figure shows the image of electron flow when no magnetic field is applied to sample and hence, no magnetic focusing signal is seen. The right figure shows the image of cyclotron orbits of the electrons while the magnetic field and charge density were tuned to the first focusing peak in Figure 5.3. The dark lines on the left of both figures show the point contacts on the edge of the sample.

The image of electron flow on the first magnetic focusing peak, shown on the right of Figure 5.4 clearly shows a cyclotron orbit connecting the first to the second point contact. The tip deflects electron trajectories, creating a shadow downstream that reduces the transresistance, creating the image. When the tip is near the sample edge, it acts to increase the transresistance, perhaps by deflecting electrons bound for the edge.
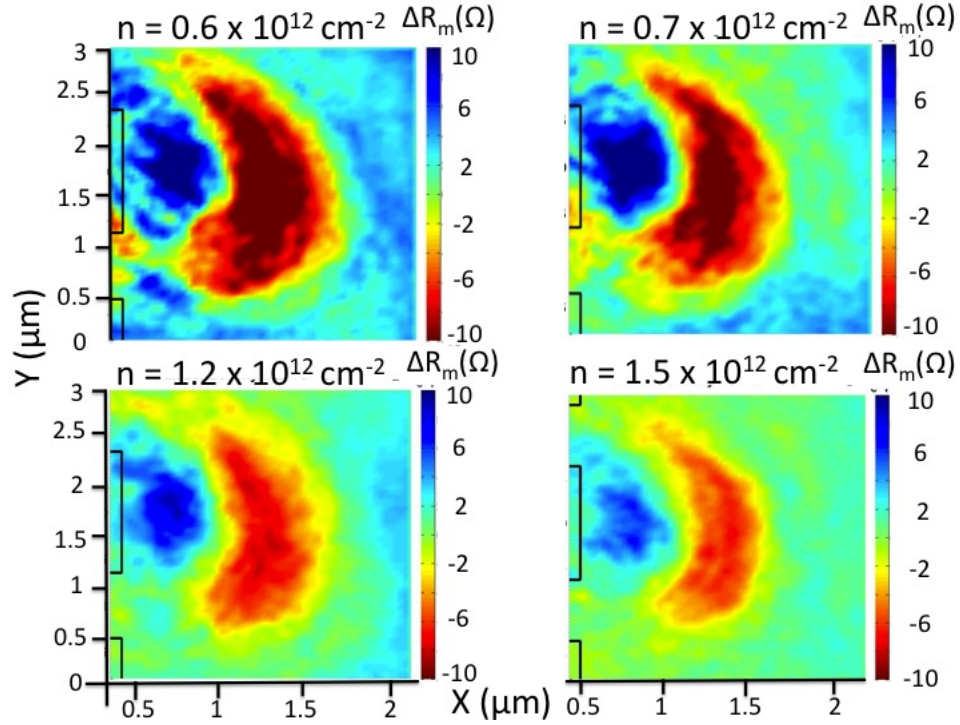


Figure 5.5: Images of electron flow during magnetic focusing on the first focusing peak at different densities. The top left figure corresponds to the lowest density, $n = 0.6 \times 10^{12} cm^{-2}$ with $B_f = 0.089$T and the top right is $n = 0.8 \times 10^{12} cm^{-2}$ and $B_f = 0.099$T. The bottom left and right correspond to densities of $n = 1.2 \times 10^{12} cm^{-2}$ with $B_f = 0.107$T and $n = 1.5 \times 10^{12} cm^{-2}$ with $B_f = 0.125$T respectively.

Figure 5.5 shows images of electron flow for magnetic focusing at first focusing field at different densities. The top left figure corresponds to the lowest density, $n = 0.6 \times 10^{12} cm^{-2}$ with $B_f = 0.089$T and the top right is $n = 0.8 \times 10^{12} cm^{-2}$ and $B_f$

$= 0.099$T. The bottom left and right correspond to densities of $n = 1.2 \times 10^{12} cm^{-2}$ with $B_f = 0.107$T and $n = 1.5 \times 10^{12} cm^{-2}$ with $B_f = 0.125$T respectively. The tip has a stronger effect on electron flow at lower electron density, as expected.
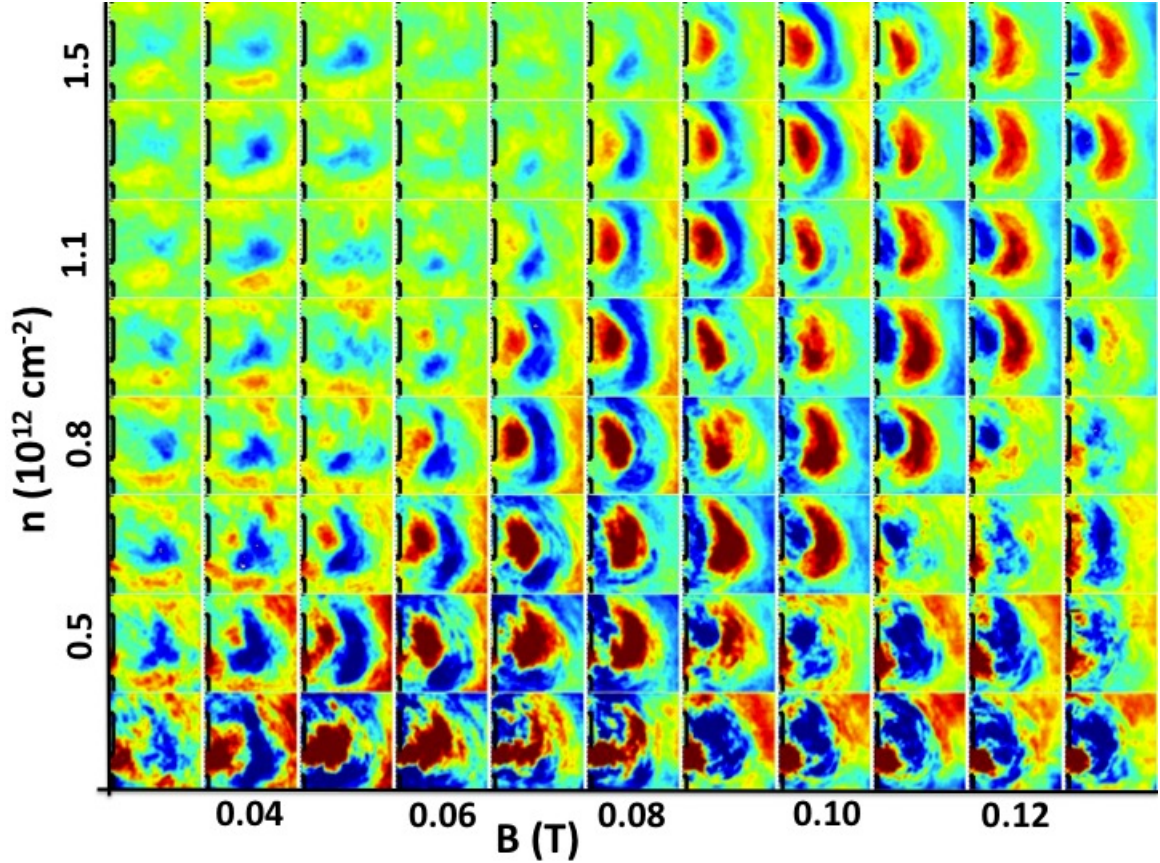


Figure 5.6: This figure shows the tiled plots of the trans-resistance maps as we vary both magnetic field B and density of charge carriers n. The magnetic field B is varied along the x-axis while the density n is varied along the y-axis. For the B and n values that correspond to the first focusing peak in Figure 5.3, we see the cyclotron orbits in the trans-resistance map. At low magnetic field, the cyclotron orbits (red regions) are close to the edge. As the magnetic field increases, the cyclotron orbits(red regions) move further away from the edge and attain a well defined shape. At high field, the cyclotron orbits disappear.

Figure 5.6 shows the tiled plots of the trans-resistance maps as as the magnetic field is increased from 0.020 T to 0.125 T, and the density is increased from 0.3 $\times$

$10^{12}$ to $1.6 \times 10^{12}$ cm$^{-2}$. The magnetic field (B) is varied along the x-axis while the density (n) is varied along the y-axis. For B and n values that correspond to the first focusing peak in Figure 5.3, we see the cyclotron orbits in the trans-resistance map. At low magnetic field, the cyclotron orbits (red regions) are close to the edge. As the magnetic field increases, the cyclotron orbits (red regions) move further away from the edge and attain a well defined shape. At high field, the cyclotron orbits disappear. This can be explained by the classical picture of electron trajectories in magnetic field. At low field, the cyclotron radius is huge and the electron trajectories that can make it from point contact 1 to point contact 3 are close to the edge. As the B-field is increased, the cyclotron radius becomes smaller and the trajectories from point contact 1 to 3 become further away from the edge as described in Section 5.4.

## 5.4 Discussion of Results

In this section we discuss the results we obtained using scanning gate microscopy technique to image the magnetic focusing of electrons in graphene. Using a simple classical model of electron motion, we justify the results we obtain in the imaging of electron flow for magnetic focusing.

As shown in Figure 5.5, the magnitude of trans-resistance increases as the Fermi level is lowered. This can be explained by simple model of tip-induced potential bump in the sample which deflects the electron trajectories producing a change in trans-resistance signal. The tip-induced potential takes a shape of Lorentzian with

induced charge density $n_i$ on the sample surface give by the following equation.

$$n_i(r) = \frac{-qa}{2\pi(r^2 + a^2)^{\frac{3}{2}}} \tag{5.3}$$

where r is the distance from the center of the tip, 'a' is tip height and 'q' is the charge on the tip. See [38] for more details on the tip-induced potential. Figure 5.7 illustrates the effect of tip-induced potential on electron trajectories as the fermi-level is changed in the sample.
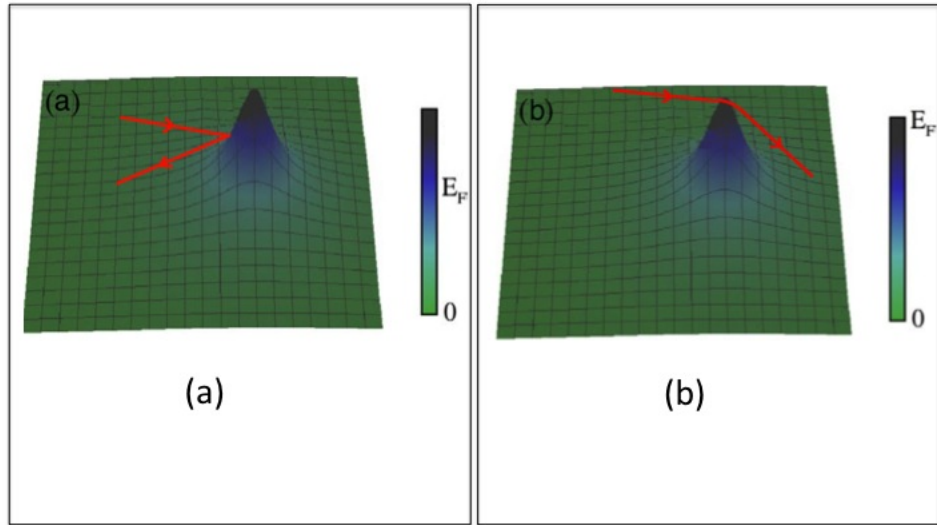


Figure 5.7: This figure shows the effect of a change in Fermi level on the scattering of electrons due to the tip-sample potential. A negative potential between the tip and the sample creates a dip in the electron density locally. Figure (a) illustrates when the electron density is low, the Fermi level is much smaller than the tip-sample potential. Figure (b) shows that at high electron density, the Fermi level is comparable to the tip-sample potential.

Figure 5.7 shows the effect of a change in Fermi level on the scattering of electrons due to the tip-sample potential. A negative potential between the tip and the sample

creates a dip in the electron density locally. Figure (a) shows that at low electron density, the Fermi level is much smaller than the tip-sample potential. This creates a dip in electron density comparable to the unperturbed density. Figure (b) shows that at high electron density, the Fermi level is comparable to the tip-sample potential. This creates a dip in electron density small compared to the unperturbed density. This qualitatively justifies the higher magnitude of $\delta R_m$ at low density compared to that at high density as seen in Figure 5.5.
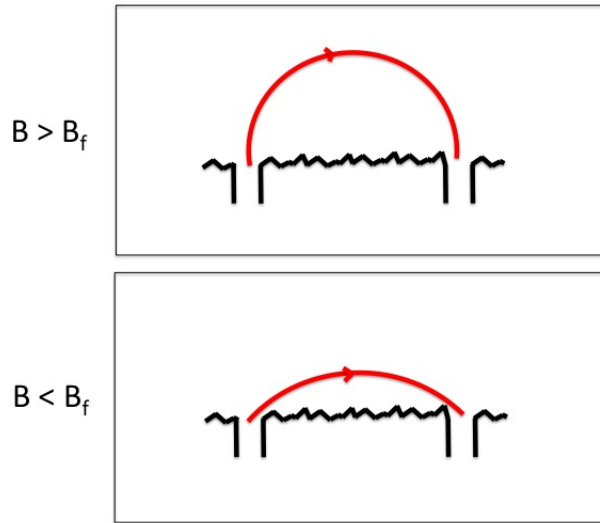


Figure 5.8: The cyclotron radius of the electron trajectories is determined by the magnetic field. In the bottom figure, the magnetic field is low compared with the first magnetic focusing peak but close to the focusing field which gives a relatively large cyclotron radius for electrons. In this case, the only electrons that can make it from point contact 1 to point contact 3 without scattering must follow a path very close to edge of the sample as illustrated. In the top figure, the magnetic field is higher but close to the focusing field which gives a smaller cyclotron radius for electrons. In this case, the only electrons that can make it from point contact 1 to point contact 3 without scattering must follow a path far from the edge of the sample as illustrated.

The field dependence of the spatial trans-resistance images is shown in Figure 5.6. At lower fields $(B << B_f)$ and higher fields $(B >> B_f)$, there is absence of cyclotron

orbits in the spatial trans-resistance images. As B is increased, the cyclotron orbits (red region) start appearing in the images. It can be noticed that the red region is closer to edge at lower fields and starts moving further away from the edge as the magnetic field is increased. This observation can be justified using a simple picture of classical trajectory of electron in magnetic field.

As shown in Figure 5.8, the cyclotron radius of the electron trajectories is determined by the magnetic field. At higher fields, the radius is smaller and vice-versa. Since the trans-resistance signal corresponds to the number of electrons that are able to reach from point contact 1 to point contact 3, only electron trajectories that do so are accountable for high electron transmission in the red region. In the bottom of Figure 5.8, the magnetic field is below but close to the focusing field. In this case, the only electrons that can make it from point contact 1 to point contact 3 without scattering must follow a path very close to edge of the sample as illustrated. In the top figure, the magnetic field is higher but close to the focusing field which gives a smaller cyclotron radius for electrons. In this case, the only electrons that can make it from point contact 1 to point contact 3 without scattering must follow a path far from the edge of the sample as illustrated.

From Figure 5.6, it can also be noticed that there is a blue region in the trans-resistance images. That corresponds to the enhancement of the trans-resistance due to the tip-induced potential. This means that electrons that would not make it from point contact 1 to point contact 3 in absence of tip, are assisted by the tip-induced potential to reach point contact 3. As seen on Figure 5.6, at lower field the blue region is far from the edge while at higher fields it appears very close to the edge

of the sample. This observation suggests that the tip enhances the transmission by deflecting electrons away from the sample edge.

Figure 5.9 present schematic diagrams that show the effect of the tip on cyclotron orbits (upper curve) for magnetic fields $B > B_f$ above the magnetic focusing field $B_f$ and (lower panel) $B < B_f$. The top figure shows the electron trajectories at relatively high B but close to the focusing field. Not all the electron trajectories can make it to from point contact 1 to point contact 3 and the ones that don't, mostly get scattered off the edges. The reflection of electrons along a smooth graphene edge is specular but due to the roughness on the edge of fabricated sample, the electrons bounce off at different directions. These electrons that bounce off the edge likely do not make it to point contact 3. In presence of the tip, such electron trajectories could get reflected off the tip-induced potential and end up in point contact 3. Therefore, the tip-induced potential could assist the electrons near the edge of the sample to make it to point contact 3 enhancing the trans-resistance. This could be one explanation of why we see the blue region of assisted transmission between the two point contacts closer to the edge at high magnetic field in Figure 5.6.

The bottom figure in Figure 5.9 illustrates the electron trajectories at low B but close to the focusing field. At low B-field, the cyclotron radius is small and the electron trajectories that cannot make it to from point contact 1 to point contact 3 are mostly taking a long trajectories as shown. These electrons that take this long path likely do not make it to point contact 3. In presence of the tip, such electron trajectories could get reflected off the tip-induced potential and end up in point contact 3 as shown in right bottom right figure. Therefore, the tip-induced potential could assist

the electrons far from the edge of the sample to make it to point contact 3 enhancing the trans-resistance. This could be one explanation of why we see the blue region far from the edge at low magnetic field.
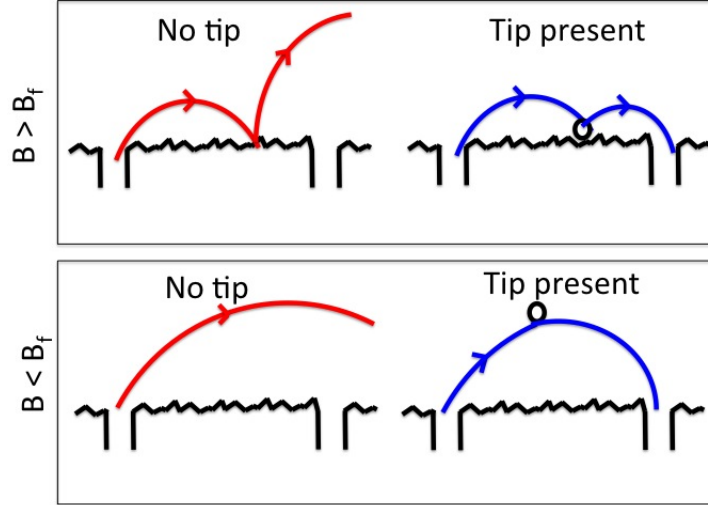


Figure 5.9: Schematic diagrams that show the effect of the tip on cyclotron orbits (upper panel) for a perpendicular magnetic field B > $B_f$ above magnetic focusing field $B_f$, and (lower curve) for B < $B_f$.

## 5.5   Conclusion

From the experiment on imaging magnetic focusing of electrons in graphene, several conclusions can be made. Rapid progress in the quality of graphene devices has made it possible to perform experiments on electron motion in ballistic regime. One of such experiments is transverse magnetic focusing of electrons in graphene. The mean free path of electrons in these devices is a few microns and having a injector and collector at comparable separation makes it possible to perform such focusing experiments. A Hall bar geometry sample can be used for this experiment. The magnetic

field focuses a current $I_i$ injected from one point contact into another point contact located an integer number of cyclotron diameters away and the build up of electrons creates a voltage $V_c$. The degree of focusing can be measured in the transresistance $R_m = V_c/I_i$.

Using cooled scanning gate microscope technique, ballistic motion of electrons in magnetic field can be imaged. In presence of magnetic field, electrons follow cyclotron motion. Placing the conducting tip of a scanned probe microscope just above the sample surface, and an applying a tip-to-sample voltage creates an image charge on the sample. This image charge can be moved while the transresistance between two point contacts is measured. The tip deflects the electrons from their original path, and thereby changing the trans-resistance between the point contacts. Such trans-resistance values for each tip position gives information about the trajectories of electrons in the sample. In our experiment, we observe cyclotron orbits owing to decrease in the transmission of electrons between the point contacts. We also observe the enhancement of transmission of electrons by the tip suggesting that the tip-induced potential could assist electron paths into the collector. The B and n dependence of the cyclotron orbits agree qualitatively with a basic geometrical model of electron trajectories. Theoretical simulations of the patterns of electron flow need to be done to quantitatively compare the theory and experimental results.

# Chapter 6

# Summary and Future experiments

The ability to electrically and mechanically manipulate samples mounted in the cooled scanning probe microscope is critical for its operation. This motivated my work on improving the Low temperature Scanning Probe Microscope. The objective of the improvements made in the microscope was to facilitate the positioning of tip and sample at helium temperature.

The microscope assembly, x, y and z feedthroughs and the insert were redesigned to incorporate the low temperature coarse positioning system. The coarse positioning system relies on the vertical motion of two wedges. The wedge pieces slide against the upper head that contains the tip holder forcing it to move sideways relative to lower head. This results in an in-plane movement of the tip holder which is clamped onto the upper head. The vertical motion of two wedges is achieved by turning two screws which are attached to the x and y feedthroughs. A range of several hundred microns can easily be achieved at low temperature using this improved system.

In this new system, I worked on incorporating a scanning capacitance microscopy

technique. This involved designing a cooled preamplifier based on HEMT FETs along with low noise AC and DC voltage supply boxes. Experimental and simulation results suggest that the technique can image local capacitance with a spatial resolution of 100 nm when the scan is performed with the tip 20 nm above the sample surface, with a tip diameter of 1 um. The noise level of the preamp circuit is $0.1e/\sqrt{Hz}$. Future experiments using this setup would be to image electronic density profiles along graphene edges or quantum dots. It could equally be used to obtain a high-resolution two-dimensional image of local change in capacitances in other materials.

The new low temperature coarse positioning system shortened the time to perform experiments because once the sample was cooled, it was never necessary to warm it up to realign the tip position. Using this setup, we were able to perform the experiment on imaging magnetic focusing of electrons in grapheme. With collaboration with Gil-Ho Lee, a post-doctoral fellow in Kim lab, we obtained high quality graphene devices encased by two hexagonal BN layers on a $Si/SiO_2$ substrate. The mean free path of electrons in these devices is few microns and having a injector and collector at comparable distance makes it possible to perform magnetic focusing experiments.

Using cooled scanning gate microscopy technique, the ballistic motion of electrons in magnetic field was imaged. In presence of magnetic field, electrons follow cyclotron trajectories. In our experiment, we observe cyclotron orbits owing to decrease in the transresistance between the two point contacts. We also observe the enhancement of transmission between the two point contacts by the tip suggesting that the tip-induced potential could assist electron paths into the collector. The B and n dependence of the cyclotron orbits agree qualitatively with basic geometrical model of electron

trajectories. Further simulation needs to be done to quantitatively compare the theory and experimental results.

Many experiments are now possible with these SPM systems. Using the scanning capacitance technique, experiments on imaging quantum hall states in 2DEGs such as graphene could be possible. It would be interesting to look at quantum dots in graphene and other exotic materials such as $MoS_2$. With collaborative efforts with Kim lab, there would be many imaging experiments on new materials that could be performed. Using the scanning gate microscope, an immediate experiment would be to look for coherent electron waves properties such as interference fringes. I have been collaborating with Gil-Ho Lee to reduce the lead size and have the flow restricted to a few modes. I hope to see excellent images result from these collaborations that would provide us with new insight on the materials and look forward to working together with the younger students in the lab.

# Bibliography

[1] M.A. Topinka, B.J. LeRoy, S.E.J. Shaw, E.J. Heller, R.M. Westervelt, K.D. Maranowski, and A.C. Gossard. Imaging coherent electron flow from a quantum point contact. *Science*, 289(5488), 2000.

[2] M.A. Topinka, B.J. LeRoy, R.M. Westervelt, S.E.J. Shaw, R. Fleischmann, E.J. Heller, K.D. Maranowski, and A.C. Gossard. Coherent branched flow in a two-dimensional electron gas. *Nature*, 410(6825), 2001.

[3] B.J. LeRoy, M.A. Topinka, R.M. Westervelt, K.D. Maranowski, and A.C. Gossard. Imaging electron density in a two-dimensional electron gas. *Applied Physics Letters*, 80(23), 2002.

[4] B.J. LeRoy, A.C. Bleszynski, K.E. Aidala, R.M. Westervelt, A. Kalben, E.J. Heller, S.E.J. Shaw, K.D. Maranowski, and A.C. Gossard. Imaging electron interferometer. *Physical Review Letters*, 94(12), 2005.

[5] P. Fallahi, A.C. Bleszynski, R.M. Westervelt, J. Huang, J.D. Walls, E.J. Heller, M. Hanson, and A.C. Gossard. Imaging a single-electron quantum dot. *Nano Letters*, 5(2), 2005.

[6] K.E. Aidala, R.E. Parrott, T. Kramer, E.J. Heller, R.M. Westervelt, M.P. Hanson, and A.C. Gossard. Imaging magnetic focusing of coherent electron waves. *Nature Physics*, 3(7), 2007.

[7] M.P. Jura, M.A. Topinka, L. Urban, A. Yazdani, H. Shtrikman, L.N. Pfeiffer, K.W. West, and D. Goldhaber-Gordon. Unexpected features of branched flow through high-mobility two-dimensional electron gases. *Nature Physics*, 3(12), 2007.

[8] A.E. Gildemeister, T. Ihn, R. Schleser, K. Ensslin, D.C. Driscoll, and A.C. Gossard. Imaging a coupled quantum dot-quantum point contact system. *Journal of Applied Physics*, 102(8), 2007.

[9] A.C. Bleszynski-Jayich, F.A. Zwanenburg, R.M. Westervelt, A.L. Roest, E.P.A.M. Bakkers, and L.P. Kouwenhoven. Scanned probe imaging of quantum dots inside InAs nanowires. *Nano Letters*, 7(9), 2007.

[10] A.C. Bleszynski-Jayich, L.E. Froberg, M.T. Bjork, H.J. Trodahl, L. Samuelson, and R.M. Westervelt. Imaging a one-electron InAs quantum dot in an InAs/InP nanowire. *Physical Review B*, 77(24), 2008.

[11] E.E. Boyd, K. Storm, L. Samuelson, and R.M. Westervelt. Scanning gate imaging of quantum dots in 1D ultra-thin InAs/InP nanowires. *Nanotechnology*, 22(18), 2011.

[12] M. Bockrath, W.J. Liang, D. Bozovic, J.H. Hafner, C.M. Lieber, M. Tinkham, and H.K. Park. Resonant electron scattering by defects in single-walled carbon nanotubes. *Science*, 291(5502), 2001.

[13] M.T. Woodside and P.L. McEuen. Scanned probe imaging of single-electron charge states in nanotube quantum dots. *Science*, 296(5570), 2002.

[14] J. Berezovsky, M.F. Borunda, E.J. Heller, and R.M. Westervelt. Imaging coherent transport in graphene (part I): mapping universal conductance fluctuations. *Nanotechnology*, 21(27), 2010.

[15] J. Berezovsky and R.M. Westervelt. Imaging coherent transport in graphene (part II): probing weak localization. *Nanotechnology*, 21(27), 2010.

[16] M.R. Connolly, K.L. Chiou, C.G. Smith, D. Anderson, G.A.C. Jones, A. Lombardo, A. Fasoli, and A.C. Ferrari. Scanning gate microscopy of current-annealed single layer graphene. *Applied Physics Letters*, 96(11), 2010.

[17] S. Schnez, J. Guettinger, M. Huefner, C. Stampfer, K. Ensslin, and T. Ihn. Imaging localized states in graphene nanostructures. *Physical Review B*, 82(16), 2010.

[18] K.S. Novoselov, A.K. Geim, S.V. Morozov, D. Jiang, Y. Zhang, S.V. Dubonos, I.V. Grigorieva, and A.A. Firsov. Electric Field Effect in Atomically Thin Carbon Films. *Science*, 306(5696), 2004.

[19] L. D. Landau. Zur Theorie der phasenumwandlungen II. *Phys. Z. Sowjetunion*, 11:26–35, 1937.

[20] R. Peierls. Quelques proprits typiques des corps solides. *Annales de l'institut Henri Poincar*, 5(3):177–222, 1935.

[21] P. R. Wallace. The band theory of graphite. *Phys. Rev.*, 71:622–634, May 1947.

[22] A. H. Castro Neto, F. Guinea, N. M. R. Peres, K. S. Novoselov, and A. K. Geim. The electronic properties of graphene. *Rev. Mod. Phys.*, 81:109–162, Jan 2009.

[23] A.K. Geim and K.S. Novoselov. The rise of graphene. *Nature Materials*, 6(183-191), 2007.

[24] Y. Zhang, Tan Y.W., H.L. Stormer, and P. Kim. Experimental Observation of the quantum hall effect and Berry's phase in graphene. *Nature*, 438:201–204, 2005.

[25] K.S. Novoselov, E. McCann, S.V. Morozov, V.I. Fal'ko, M.I. Katsnelson, U. Zeitler, D. Jiang, F. Schedin, and A.K. Geim. Unconventional quantum Hall effect and Berry's phase of 2 pi in bilayer graphene. *Nature Physics*, 2:177–180, 2006.

[26] M.I. Katsnelson, K.S. Novoselov, and A.K. Geim. Chiral tunneling and the Klein paradox. *Nature Physics*, 2(620-625), 2006.

[27] J. Martin, G. Akerman, G. Ulbricht, T. Lohmann, J.H. Smet, K.von Klitzing, and A. Yacoby. Observation of electron-hole puddles in grapheme using a scanning single-electron transistor. *Nature Physics*, 4(144-148), 2008.

[28] G.Z. Magda, X. Jin, I. Hagymasi, P. Vansco, Z. Osvath, N. Nemes-Incze, C. Hwang, L.P. Biro, and L. Tapaszto. Room-temperature magnetic order on zigzag edge of narrow graphene nanoribbons. *Nature*, 514:608–611, 2014.

[29] A. Rycerz, J. Tworzyd, and C.W.J. Beenakker. Valley filter and valley valve in graphene. *Nature Physics*, 3(172-175), 2007.

[30] S. V. Morozov, K. S. Novoselov, M. I. Katsnelson, F. Schedin, L. A. Ponomarenko, D. Jiang, and A. K. Geim. Strong Suppression of Weak Localization in Graphene. *Physical Review Letters*, 97(1):016801+, July 2006.

[31] P. Recher, B. Trauzettel, A. Rycerz, Ya, C. W. J. Beenakker, and A. F. Morpurgo. Aharonov-Bohm effect and broken valley degeneracy in graphene rings. *Physical Review B*, 76(23):235404+, December 2007.

[32] C. R. Dean, A. F. Young, I. Meric, C. Lee, L. Wang, S. Sorgenfrei, K. Watanabe, T. Taniguchi, P. Kim, K. L. Shepard, and J. Hone. Boron nitride substrates for high-quality graphene electronics. *Nature Nanotechnology*, 5(10):722–726, August 2010.

[33] K.I. Bolotin, F. Ghahari, M.D. Shulman, and P. Kim. Observation of the fractional quantum Hall effect in graphene. *Nature*, 462:196–199, 2009.

[34] A.F. Young and P. Kim. Quantum interference and Klein tunneling in graphene heterojunctions. *Nature Physics*, 5:222–226, 2009.

[35] T. Taychatanapat, K. Watanabe, T. Taniguchi, and P. Jarillo-Herrero. Electrically tunable transverse magnetic focusing in graphene. *Nature Physics*, 9(225-229), 2013.

[36] G. Steele. *Imaging Transport resonances in the quantum hall effect.* PhD thesis, M.I.T, 2006.

[37] R.C. Ashoori. Electrons in artificial atoms. *Nature*, 379(413-419), 1996.

[38] M.A. Topinka. *Imaging Coherent Electron Wave Flow Through 2-D Electron Gas Nanostructures.* PhD thesis, Harvard University, 2002.

[39] K.E. Aidala. *Imaging Magnetic Focusing in a Two-Dimensional Electron Gas.* PhD thesis, Harvard University, 2006.

[40] G. A. Steele, R. C. Ashoori, L. N. Pfeiffer, and K. W. West. Imaging transport resonances in the quantum hall effect. *Phys. Rev. Lett.*, 95:136804, Sep 2005.

[41] Yu.V. Sharvin and L.M. Fisher. Observation of focused electron beams in a metal. *Journal Of Experimental and Theoretical Physics Letters*, 1:152, 1965.

# Appendix A

# Pre-amplifier circuit board Fabrication and tip fabrication

This appendix is to serve as a manual for the fabrication of preamplifier circuit board as briefly discussed in previous Chapter refchap:Microscope.

## A.1    Pre-amplifier circuit board fabrication / installation

1. Use the jeweler's mill to machine a single preamp pcb out of the circuit board that has array of preamp circuits. The size of the resulting single preamp pcb should be approximately 14mm x 16 mm as shown in Figure 4.2.

2. Use the fine soldering station to carefully solder the $470K\Omega$, $10M\Omega$ and $1K\Omega$ resistors. Solder the 100 pF capacitor.

3. Prepare the stycast epoxy: Mix Stycast Part A to Stycast part B 10:1 in a disposable beaker and stir it for a few minutes. Leave the mixture in the fume hood for half an hour. This helps get rid of the large size air bubbles trapped in the epoxy.

4. Use the vacuum desiccator to pump out the small size air bubbles trapped in the epoxy. It typically takes about an hour to pump out all the bubbles.

5. After the epoxy is completely bubble free, use a toothpick to dab a bit of epoxy onto the locations of HEMT transistors as shown in Figure 4.2.

6. Carefully place the HEMT transistors on top of the epoxy one by one using the fine tweezers.

7. Leave the pcb for the epoxy to cure. It takes approximately 16 hours.

8. Solder wires to all the bond pads on the circuit. Use the manganin wire for this purpose. Make sure to scratch off the insulation on the end of the wire before soldering. Solder these to a Microtech connector for electrical connection to the cryostat leads.

9. Connect all the wires to ground. This would prevent from electricuting the HEMT while wire-bonding.

10. Use silver paint to stick your sample on sample loading area on the pcb.

11. Use the grounding strap to ground yourself. Load the pcb into wirebonder. Heat the pcb to 120 degree Celsius. Use a 16 micron gold wire for bonding. Carefully bond the gates, drains and sources of each of the transistors as shown in Figure 4.2.

12. Load the pcb onto the sample holder on top of the piezotube. Follow instructions on Appendix B for aligning the tip above the sample. The instructions on how to make the tips are listed in Appendix C.

## A.2   Tip Fabrication

1. We use electrochemical etching technique to make tungsten tips of few microns diameter.

2. Strip a tungsten wire of length 1 inches.

3. Prepare a 2 M solution of sodium hydroxide (NaOH).

4. Set up a simple electrolysis circuit with the tungsten wire as anode and an evaporator boat as cathode.

5. Adjust the voltage source to supply 2.00 V.

6. Bubbles should start forming in the solution,which signifies that the reduction reaction is occurring.
Anode: $W(s) + 6OH^- \rightarrow WO_3(s) + 6e^- + 3H_2O$ and
$WO_3(s) + 2OH^- \rightarrow WO_4^{2-}(aq) + H_2O$
Cathode: $6H_2O + 6e^- \rightarrow 3H_2(g) + 6OH^-$

7. Watch for the tungsten wire to etch away. A kink should start forming and as soon as the bottom part falls off, remove the tip from solution.

8. Using fine tweezers, place the top part in acetone and methanol before blow-drying. Be careful not to have the tip touch any surface as it can contaminate the tip or make it blunt.

9. Obtain an image of the tip using scanning-electron microscopy before use to ensure its usability.

# Appendix B

# Head Assembly and Room Temperature Alignment Procedure

This appendix is to serve as a manual for the installation of a sample and alignment of the tip. The assembling of the piezotube and cage are discusses in Kathy's thesis and this manual would be useful after the piezotube and cage are assembled. Also, it is assumed that we are using a doped Silicon backgate sample. It is critical to keep yourself and the sample grounded throughout this process so that the sample doesn't get electrocuted due to static discharge.

1. Cut a small piece of aluminum foil (bigger than your sample) and paste it using conductive silver paste onto the sample holder. Use the flat end of a toothpick to flatten out the aluminum foil. Wait for 15 minutes to let the silver paste dry. Wipe out any excess silver paste from the side of the aluminum foil.

2. Scratch the backside of the Silicon device and apply some conductive Silver paste. Attach the device gently onto the aluminum foil. Apply gentle pressure on all four corners of the device so that the device sits flat on the aluminum foil. Leave it to dry for 15 minutes.

3. Wirebond the sample bondpads to the chip carrier pads. If the CNS wirebonder is used, have the power set between 150 and 180 mW for the second bond while 350 mW for the first bond. A sonication time of 15 ms is usually sufficient. Typically, using higher power for the bond creates issues of gate leakage on the sample.

4. Carefully, attach the sample chip carrier to the piezotube chip carrier plate.

   a. Insert two 0-80 screws in the aligned sample chip carrier and piezotube grounding plate. It's important to align the sample holder such that the leads are coming out towards the z-positioning screw on the cage assembly.

    b. Use a small screw driver to secure the chip carrier onto the piezotube. The screws should be finger-tight to avoid stressing the piezotube too much during attachment.

    c. Use dental floss to tie the sample leads onto the cage assembly. Typically, two ties at top and bottom of cage assembly would be sufficient.

5. Install the cantilever tip.

    a. Use a handheld multimeter to measure the resistance of the cantilever to confirm that the cantilever is not broken. It should read around 650 to 700 ohms.

    b. Wirebond the cantilever connections to the corresponding bondpads on the cantilever chip carrier. This is to ensure that there is a connection to the cantilever even when the original wired connection breaks at cold temperature.

    c. Measure the resistance of the cantilever again to make sure it still is safe.

6. Install the head assembly.

    a. Place the cantilever chip on top of the tip holder.

    b. Solder the leads onto the bondpads of cantilever chip carrier.

    c. Before placing the head assembly on top of the cage assembly make sure the $z$ ball end screw on the cage is at least 2 mm higher than the remaining two ball end screws.

    d. Place the head assembly on top of cage such that the grooves align well with the three ball end screws on the cage assembly.

    e. Use spring hooks to attach the head assembly firmly onto the cage.

    f. Use dental floss to tie the cantilever wires on the cage assembly.

7. Align the $x$, $y$ and $z$ position of the tip at room temperature.

    a. Use the long working distance binocular microscope to view the position of the sample and tip.

    b. Lie the microscope in a cradle so that the microscope is tilted and start lowering the tip closer to the sample until you can see the tip end almost touches its shadow. This would mean that tip is very close to the sample surface.

    b. Bring the tip off the surface by turning the $z$ approach ball end screw one full rotation clockwise.

    c. Take the microscope off the cradle and place it vertical. Adjust the focus to view the sample and tip.

    d. Loosen the clamp that holds the tip holder slightly by unscrewing the $0-80$ screws.

    e. Use a screw to slide the tip holder for aligning the tip within the lithographically written number grid pattern on the sample.

    f. Tighten the clamp to fix the tip holder in place.

8. Prepare microscope for insertion.

    a. Place the microscope upside down into the insert. Make sure to allow some slack when screwing the microscope into the insert.

    b. Check the orientation of the $x$ and $y$ positioning flat head drivers and the screws on the head assembly. Make sure to align them properly.

    c. Loosen the z-approach rod by unscrewing it from the top part. Slide it down and turn it until you find the match between the rod and the ball end screw.

    d. Secure the screws that hold the microscope to the insert.

    e. Secure the z-approach rod to the top section of z feedthrough in the insert.

    f. Connect all the sample leads from the insert into the sample holder leads. Connect the cantilever leads and the high voltage lines for the piezotube to the corresponding leads in the insert.

    g. Use dental floss to secure all the wires on the microscope.

    h. Carefully insert the brass tube into the microscope. Make sure to look out for wires getting caught or stuck while sliding up the tube.

    i. Secure the tube to the insert.

    j. Slowly slide the probe shield tube into the insert. Secure it firmly with the KF-40 clamp. The microscope is now ready for room temperature scanning and measurement.

# Appendix C

# Cooling the Microscope to Helium Temperature

This appendix is to serve as a manual for the cooling the microscope to Helium temperature.

## C.1 Evacuate the probe shield

1. With the assembled microscope held upside down in the insert, it's important to find the location of tip relative to the sample before moving any further in the experiment.

2. Perform a room temperature topographical scan as described in Leroy's thesis. Once the alignment of the tip is known, if the tip is too far from the sample, coarse positioning can be performed without having to take the microscope out of the insert. Use the *xandy* positioning knobs at the top to align the tip relative to the sample. Ideally, the tip should be brought 8 half turns off the surface for alignment.

3. Once the tip is aligned, the microscope shield is ready to be evacuated and filled with exchange gas for cooling.

4. Attach the vacuum T connector to the probe shield.

5. Attach the needle valve (LV10K from edwards vacuum parts) to the T.

6. Use a thin transparent tube for connecting the valve to the cryostat. The helium boil off from the cryostat will be used as a source of exchange gas later.

7. Connect the remaining port of the T to the Pfeiffer vacuum system.

8. Open the valve in the Pfeiffer vacuum and the probe shield. Start the pump. Pump it down to $10^{-6}$ mbar. Leaving it to pump overnight would be sufficient.

9. Once the vacuum has reached $10^{-6}$ mbar, close the valve on the pump. Turn off the pump.

10. Open the needle valve slowly to let the helium boil off flow into the probe shield. When the pressure is reached to 2 mbar, gently close the needle valve and the valve on the probe shield.

11. Detach the tube connected to the probe shield from pump. Detach the tube connected to the cryostat for Helium inlet. Put a cap on the probe valve and clamp it down.

12. The microscope is now ready to be cooled down.

## C.2    Cooling the microscope

1. Before beginning the cooling procedure, make sure the cryostat has full helium. This would give maximum time for aligning the tip and doing the measurement at helium temperature before the cryostat needs another refill. Once refilled, the tip can drift a few microns off.

2. Gently lift the microscope using the hoist. It's important to avoid abrupt jumps so that the tip doesn't drift too much.

3. Position the NW/KF compression coupler about a feet and a half above the bottom end of the microscope. Tighten it securely.

4. Open the valve in cryostat to release the pressure.

5. Open the KF-40 flange on top and gently lower the microscope into the cryostat. Stop when the NW/KF compression coupler touches the KF-40 flange in the cryostat. Clamp down the coupler into the KF-40 flange.

6. Leave the microscope at this position for a couple of hours until the temperature is stable. Leaving it at this state overnight would be sufficient.

7. Gently lower the microscope a few inches every hour until the microscope can go no further inside the cryostat. The microscope is now ready for low temperature measurement.

# Appendix D

# Sample Fabrication

This appendix is to serve as a manual for making hBN-graphene-hBN heterostructures.

1. Two chips of hexagonal boron nitride and one of graphene are required for the stacking process. Using standard mechanical exfoliation technique, graphene is isolated on Silicon wafer and identified as such via Raman microscopy. Graphene should have at least an area of 25 square micrometers in order to achieve a good usable area for measurement.

2. Using similar cleaving proves, Boron nitride chips with area large enough to accommodate graphene are identified using optical microscope. Once big enough chips are found, using atomic force microscope the flatness and thickness of these chips are measured. A BN with large enough flat region and thickness ranging from 20-60 nm is chosen for our stacking process.

3. Poly Propylene Carbonate (PPC) dissolved in anisole is the polymer that will be used for this pickup process. The PPC solution is spin coated on silicon wafer at 3000 rpm for 90 seconds and then baked for five minutes at $90°C$.

4. Prepare PDMS on a petri dish. Cut a 3mm x 3mm piece of PDMS and place it atop a glass slide. Apply transparent packing tape to secure the PDMS in place.

5. Punch a circular hole (larger than the size of PDMS piece) on a scotch tape. Apply the tape on the previously PPC coated wafer and peel off the PPC layer. Gently, deposit the polymer layer on top of the PDMS square on the glass slide such that the circular window covers the PDMS.

6. Heat the glass slide with PPC/PDMS (transfer slide) to $60°C$ to get rid of any wrinkles that may be present on the polymer.

7. Identify a boron nitride chip for pickup. This would be the BN that would eventually be the top layer in our layered structure. Secure the device on sample holder of the transfer stage.

8. Clamp the transfer slide on to the probe arm of the transfer stage. Use the micro-manipulator controls to align the PPC/PDMS square over the BN chip. Ideally, the BN should be centered on the square.

9. Slowly, lower the transfer arm using the z positioning control of the transfer arm until it makes soft contact with the BN chip. Ripples with start to appear originating from the point of contact and ideally we want point of contact fairly close to the BN chip to be picked up.

10. Once the contact is satisfactory, heat the wafer to around $70°C$ raising the temperature by a degree every few minutes. At this point, all BN chip should be in complete contact with the PPC.

11. Cool the wafer down to room temperature.

12. Using the z positioning control of the transfer arm, gently lift the PPC up. Make sure that the wavefront of contact is moving slowly when lifting.

13. Once the polymer layer is clear from the wafer, check to determine if the boron nitride chip in question is still on the silicon  if not, the pick-up step was a success.

14. Next step is to pick up graphene. This time align the boron-nitride on PPC (on the transfer arm) atop the graphene on silicon and repeat the steps above.

15. The final transfer step involves aligning the graphene-on-boron nitride-on PPC stack atop the remaining boron nitride wafer.

16. Once the graphene-on-boron nitride is aligned, lower the transfer arm until there is soft contact. Ensure that the origin of ripples is close to the chips.

17. Heat the wafer to around $110°C$ raising the temperature by a degree every few minutes. Once the temperature has reached $110°C$, the PPC should be completely melted and therefore while lifting up the transfer arm, the PPC in contact should be left on the wafer. This would leave BN-graphene-BN layered device on the wafer along with the PPC.

18. Leave the device in acetone overnight. Use standard Acetone and IPA to wash off any residues left. Blow dry the sample using Nitrogen gun.

19. Heat the sample unto $300°C$ in vacuum to get rid of any residue that might be still left.

20. The sample is now ready for electron-beam lithography.